

New insights and coupled modelling of the structural and thermodynamic properties of the LiF-UF₄ system

Ocádiz-Flores, J. A.; Gheribi, A. E.; Vlieland, J.; Dardenne, K.; Rothe, J.; Konings, R. J.M.; Smith, A. L.

DOI

[10.1016/j.molliq.2021.115820](https://doi.org/10.1016/j.molliq.2021.115820)

Publication date

2021

Document Version

Final published version

Published in

Journal of Molecular Liquids

Citation (APA)

Ocádiz-Flores, J. A., Gheribi, A. E., Vlieland, J., Dardenne, K., Rothe, J., Konings, R. J. M., & Smith, A. L. (2021). New insights and coupled modelling of the structural and thermodynamic properties of the LiF-UF₄ system. *Journal of Molecular Liquids*, 331, Article 115820. <https://doi.org/10.1016/j.molliq.2021.115820>

Important note

To cite this publication, please use the final published version (if applicable). Please check the document version above.

Copyright

Other than for strictly personal use, it is not permitted to download, forward or distribute the text or part of it, without the consent of the author(s) and/or copyright holder(s), unless the work is under an open content license such as Creative Commons.

Takedown policy

Please contact us and provide details if you believe this document breaches copyrights. We will remove access to the work immediately and investigate your claim.



New insights and coupled modelling of the structural and thermodynamic properties of the LiF-UF₄ system

J.A. Ocádiz-Flores^a, A.E. Gheribi^b, J. Vlieland^a, K. Dardenne^c, J. Rothe^c, R.J.M. Konings^{a,d}, A.L. Smith^{a,*}

^a Delft University of Technology, Faculty of Applied Sciences, Radiation Science & Technology Department, Mekelweg 15, 2629, JB Delft, the Netherlands

^b Centre for Research in Computational Thermochemistry, Department of Chemical Engineering, École Polytechnique, C.P. 6079, Succursale "Downtown", Montreal, Quebec H3C 3A7, Canada

^c Karlsruhe Institute of Technology (KIT), Institute for Nuclear Waste Disposal (INE), Radionuclide Speciation Department, Hermann-von-Helmholtz-Platz 1, 76344 Eggenstein-Leopoldshafen, Germany

^d European Commission, Joint Research Centre, P.O. Box 2340, D-76125 Karlsruhe, Germany

ARTICLE INFO

Article history:

Received 3 November 2020

Accepted 26 February 2021

Available online 03 March 2021

Keywords:

CALPHAD

Molten salt reactor

Differential scanning calorimetry

X-ray diffraction

EXAFS

Polarizable ion model (PIM)

ABSTRACT

LiF-UF₄ is a key binary system for molten fluoride reactor technology, which has not been scrutinized as thoroughly as the closely related LiF-ThF₄ system. The phase diagram equilibria in the system LiF-UF₄ are explored in this work with X-ray diffraction (XRD) and differential scanning calorimetry (DSC). The short-range ordering in the molten salt solution is moreover surveyed with Extended X-ray Absorption Fine Structure spectroscopy (EXAFS) and interpreted using a combination of standard fitting of the EXAFS data and Molecular Dynamics (MD) simulations with a Polarizable Ion Model (PIM) potential. The density, excess molar volume, thermal expansion, heat capacity, and enthalpy of mixing are extracted from the MD simulations across a range of temperatures and compositions; the behavior is non-ideal, with reasonably good agreement with the experimental data. Also calculated is the distribution of heteropolyanions in the liquid solution, and modelled using the quasi-chemical formalism in the quadruplet approximation taking into account the existence of the single-shell complexes [UF₇]³⁻, [UF₈]⁴⁻, and the dimeric species [U₂F₁₄]⁶⁻. Subjecting the optimization of the excess Gibbs energy parameters of the liquid solution to the constraints of the phase diagram data and local structure of the melt as derived from the EXAFS and coupled MD simulations, a CALPHAD-type assessment is proposed, linking structural and thermodynamic properties, with a rigorous physical description of the melt.

© 2021 The Authors. Published by Elsevier B.V. This is an open access article under the CC BY license (<http://creativecommons.org/licenses/by/4.0/>).

1. Introduction

The Molten Salt Reactor (MSR) is a type of nuclear reactor whose main characteristic is a fuel in the liquid state that also serves as the primary coolant: a stream of molten fluorides or chlorides. The reactor was originally conceived as a candidate engine to power aircraft in the Aircraft Reactor Experiment (ARE) [1], designed, built and operated by Oak Ridge National Laboratory (ORNL) in the 1950's. Later, the potential of such reactors as a civilian power source was recognized and demonstrated during the Molten Salt Reactor Experiment (MSRE), also in ORNL in the 1960's [2]. More recently, the Generation IV International Forum, a group of fourteen member countries pursuing research and development for the next generation of nuclear reactors, has selected the MSR as one of six key nuclear energy systems to replace the current fleet of Generation II Light Water Reactors [3].

The LiF-UF₄ system was a key component of the MSRE fuel (⁷LiF-BeF₂-ZrF₄-UF₄) [4], and its phase diagram was investigated as part of the original research effort at ORNL by Barton et al. in 1958 [5]. Many

years later, in 2010, a CALPHAD (Calculation of PHase Diagram) [6] thermodynamic model of the binary system was optimized based on the experimental data from ORNL using a modified quasi-chemical model in the quadruplet approximation to describe the liquid solution [7]. This system is also critically important in the proposed fuel of future reactors, such as ⁷LiF - ThF₄-²³³UF₄ for the Molten Salt Fast Reactor (MSFR) [8], LiF - BeF₂ - ThF₄ - UF₄ for the liquid-fueled thorium molten salt reactor (TMSR-LF) [9], and the ThorCon reactor which aims to be a scale-up of the MSRE [10]. Despite this, there have been no more phase diagram data gathered since 1958 to compare with the original measurements, as it has been done extensively for other systems, e.g. LiF-ThF₄ [11].

This work gives new insights into the phase equilibria of this key system using Differential Scanning Calorimetry (DSC) combined with X-ray Diffraction (XRD) measurements.

In a wider effort to understand the structure of molten (Li,U)F_x salt and its relationship with macroscopic thermodynamic (and transport) properties which are highly relevant for reactor design and operation, in-situ high temperature Extended X-ray Absorption Fine Structure (EXAFS) spectroscopy measurements of the system are performed for the first time at high UF₄ content. They are furthermore interpreted with the help of Molecular Dynamics (MD) simulations, which have

* Corresponding author.

E-mail address: a.l.smith@tudelft.nl (A.L. Smith).

proved throughout several years already to be an invaluable tool for characterizing the thermo-physical and thermo-chemical properties of molten salts [12–15]. The structural information obtained from the EXAFS data, interpreted and extended to a wider range of temperatures and compositions using MD, is ultimately linked to the phase diagram equilibria and excess thermodynamic properties. Using both experimental and simulated data as input, a coupled structural-thermodynamic model is developed using an advanced modified quasi-chemical model in the quadruplet approximation, with a formalism similar to the recent assessment of the LiF - BeF₂ system [16].

2. Experimental methods

2.1. Reagent preparation and handling

The purity of LiF (ultra-dry from Alfa Aesar, 0.9999 ± 0.0001 mass fraction purity) and UF₄ (International Bio-Analytical Industries, 0.9999 ± 0.0001 mass fraction purity) reported by the suppliers correlated well with X-ray diffraction (XRD) and Differential Scanning Calorimetry (DSC) tests. LiF has a white color while UF₄ is green, and both were handled in either powder or pressed pellet form. The experimental compositions reported hereafter were prepared by mixing either powder or pellet fragments of the pure salts in the required stoichiometric ratios. As fluoride salts are highly sensitive to water and air, handling and preparation of samples took place inside the dry atmosphere of an argon-filled glove box, where H₂O and O₂ content were kept below 5 ppm.

The DSC heat flow signal for both LiF and UF₄ showed only one event assigned to the melting point, and no other thermal events that could be attributed to impurities. The measured onset temperatures, after correction for the effect of the heating rate, are in good agreement with the literature: (1118 ± 5 K) and (1306 ± 5 K), respectively, vs. 1121.3 K (LiF, [17]), and (1307.9 ± 3.0) K (UF₄, [18]).

2.2. Synthesis

The samples whose X-ray diffraction patterns are shown in this work were prepared by grinding powder mixtures, and heating them above melting temperatures inside a closed stainless steel crucible with a nickel liner in a tubular furnace under argon flow, with slow cooling, typically $2 \text{ K} \cdot \text{min}^{-1}$, to allow for a good re-crystallization. The specific conditions for each sample are given below in Table 1.

2.3. Powder X-ray diffraction

X-ray powder diffraction (XRD) data were collected at room temperature ($T = 293 \pm 5$ K) using a PANalytical X'Pert PRO X-ray diffractometer and a Cu anode ($0.4 \text{ mm} \times 12 \text{ mm}$ line focus, 45 kV, 40 mA) by step scanning at a rate of $0.0104^\circ \cdot \text{s}^{-1}$ in the range $10^\circ < 2\theta < 120^\circ$ in a Bragg-Brentano configuration. The X-ray scattered intensities were measured with a real time multi strip (RTMS) detector (X'Celerator). The samples were measured inside a sealed sample holder, with kapton

foil cover, maintaining the dry argon atmosphere of the glove box. Structural analysis was performed with the Rietveld and LeBail methods using the FullProf suite [19].

2.4. Differential scanning calorimetry

3D-heat flow DSC measurements were performed using a Setaram Multi-Detector HTC module of the 96 Line calorimeter under argon flow at a pressure of (0.10 ± 0.005 MPa). All samples were placed inside a nickel liner and encapsulated for the calorimetric measurements inside a stainless steel crucible closed with a screwed bolt as described in [20] to avoid vaporization at high temperatures. All measurement programs started with one heating cycle reaching ~ 1398 K and held at that temperature for 300 s (i.e. around 90 K above the fusion temperature of UF₄ as measured at $10 \text{ K} \cdot \text{min}^{-1}$ heating rate) to ensure complete mixing of the end-members and attainment of the equilibrium state. In general, this first cycle was followed by three successive heating cycles with a heating rate ranging between 4 and $10 \text{ K} \cdot \text{min}^{-1}$, and 20–15–10–5 $\text{K} \cdot \text{min}^{-1}$ cooling rates.

A series of interconnected S-types thermocouples were used to record the sample temperature throughout the experiments. The temperature on the heating ramp was calibrated by measuring the melting points of standard high purity metals (In, Sn, Pb, Al, Ag, Au), following the procedure described in [21,22], thereby ensuring the measured temperatures can be translated to the International Temperature Scale (ITS-90). The temperature on the cooling ramp was obtained by extrapolation to $0 \text{ K} \cdot \text{min}^{-1}$ cooling rate. The melting temperature of pure compounds and transition temperatures of mixtures were derived on the heating ramp as the onset temperature using tangential analysis of the recorded heat flow, while the liquidus temperature of mixtures was taken as the peak extremum of the last thermal event as recommended in [23]. The data measured on the cooling ramp were not retained for the phase diagram optimization due to the occurrence of supercooling effects, but were used to help data interpretation and identification of transition events. The uncertainty on the measured temperatures is estimated to be ± 5 K for the pure compounds and ± 10 K for mixtures.

2.5. High-temperature EXAFS measurements

EXAFS measurements were performed at the INE beamline [24] of the KARA synchrotron facility (Karlsruhe, Germany), with 2.5 GeV and 150–170 mA as operating conditions in the storage ring. The beamline uses a Ge(422) double-crystal monochromator (DCM). Rh-coated mirrors collimate and focus the beam with spot size $300 \mu\text{m} \times 500 \mu\text{m}$ at the sample position. Samples were probed at the U L₃ edge (17.166 keV), scanning from ~ 17.14 to ~ 17.77 keV. Transmission and fluorescence yield detection mode (recording the U-L_α fluorescence line by two silicon drift detectors) were applied simultaneously.

A dedicated experimental set-up, described in detail in [25], designed and built to operate at the INE beamline was used for the measurements. The set-up consists of a purpose-designed furnace inside a custom-made glovebox filled with nitrogen atmosphere. The samples

Table 1
Synthesis conditions.

Starting reagents ^a	Ramp	Hold ^b	Cooling	Composition ^c
	$\text{K} \cdot \text{min}^{-1}$	K, min	$\text{K} \cdot \text{min}^{-1}$	
(LiF:UF ₄) = (0.877:0.123)	10	1350, 30	2	Li ₃ UF ₇ + LiUF ₅
(LiF:UF ₄) = (0.75:0.25)	10	1350, 30	2	LiUF ₅ + Li ₄ UF ₈ + UF ₃
(LiF:UF ₄) = (0.5:0.5)	10	1350, 30	2	LiUF ₅
(LiF:UF ₄) = (0.2:0.8)	10	1350, 30	2	LiUF ₅ + LiU ₄ F ₁₇ + UF ₃

^a Standard uncertainty on the composition of the starting reagents was $u(X(\text{UF}_4)) = 0.005$.

^b Standard uncertainty u is $u(T) = 15$ K.

^c As determined by XRD.

(8–20 mg) were prepared in the inert atmosphere of a purified-argon glovebox by mixing and grinding stoichiometric amounts of LiF and UF₄ end-members, and then pressing pellets of thickness less than 100 μm by applying a pressure of 10 tons·cm⁻². The prepared pellets were sealed in a pre-dried boron nitride containment cell and loaded into the furnace chamber which was evacuated down to ~2·10⁻⁵ mbar to avoid reaction of the salts with residual oxygen or water.

The EXAFS data were collected ~50 K above liquidus temperature (as calculated from the CALPHAD model of Beneš et al. [7]). Short scans were made during the heating ramp to detect the melting of the material. The temperature was ramped up to the melting point of LiF and held for about 15 min to ensure complete melting and homogenization. The temperature was subsequently adjusted to a set value ~50 K above liquidus. In addition, an equilibration time of ~15–30 min was employed at the set temperature before collecting the data to ensure the signal had stabilized.

Each scan took close to 30 min, and three to four scans were accumulated to be averaged. A step size of 0.8 eV was used in the XANES region. The energy E_0 of the edge absorption threshold position was identified as the first node of the second derivative of the signal. Prior to averaging, the spectra were aligned with the XANES spectrum of a reference yttrium (K edge = 17.0384 keV) foil, located between the second and third ionization chambers and measured concurrently with the sample. EXAFS data were collected up to ~12.5 Å, and were Fourier transformed using the Hanning window over the k -range 3–9 Å⁻¹ ($dk = 2$). Data treatment (normalization and extraction) of the raw XAS data was done with ATHENA software [26], version 9.25.

3. Molecular dynamics simulations

MD simulations were performed for all compositions measured by EXAFS at the corresponding experimental temperatures, i.e. 50 K above the liquidus equilibrium. In addition, the entire composition range was studied in intervals of 0.10 X(UF₄), at temperatures in the 900–1400 K range (Table 3). The form of the potential used for the study of this molten salt system is the Polarizable Ion Model (PIM) with the general form suggested by Salanne et al. [27]. It has been chosen because it has already shown its usefulness in the study of several molten salt systems such as alkali fluoride mixtures [27], LiF-BeF₂ [15,28], AF-ZrF₄ (A = Li, Na, K) [29], and LiF-ThF₄ [30]. The potential has four contributions with functional forms given in Eq. 1 to 5: charge-charge (Eq. 1), dispersion (Eq. 2), overlap repulsion (Eq.4) and polarization (Eq.5).

- Charge-charge:

$$V_{qq}(r_{ij}) = \sum_{i<j} \frac{q_i q_j}{r_{ij}} \quad (1)$$

where q denotes the ionic formal charges.

- Dispersion:

$$V_{disp}(r_{ij}) = - \sum_{i<j} \left[f_{ij}^6(r_{ij}) \frac{C_{ij}^6}{r_{ij}^6} + f_{ij}^8(r_{ij}) \frac{C_{ij}^8}{r_{ij}^8} \right] \quad (2)$$

where $C_{ij}^6(r_{ij})$ is the dipole-dipole dispersion coefficient and $C_{ij}^8(r_{ij})$ is the dipole-quadrupole dispersion coefficient, while $f_{ij}^6(r_{ij})$ and $f_{ij}^8(r_{ij})$ are Tang-Toennies dispersion damping functions; they are short-range corrections to the asymptotic multipole expansion of dispersions [31]:

$$f_{ij}^n(r_{ij}) = 1 - e^{-b_{ij}^n r_{ij}} \sum_{k=0}^n \frac{(b_{ij}^n r_{ij})^k}{k!} \quad (3)$$

This work only consider dipoles and quadrupoles.

- Overlap repulsion

$$V_{rep}(r_{ij}) = \sum_{i<j} A_{ij} e^{-a_{ij} r_{ij}} \quad (4)$$

Here A_{ij} and a_{ij} are fitting parameters.

- Polarization

$$V_{pol}(r_{ij}) = \sum_{i<j} \left[q_i \mu_{i\alpha} g_{ij}(r_{ij}) - q_i \mu_{i\alpha} g_{ij}(r_{ij}) \right] T_{\alpha}^{(1)}(r_{ij}) - \sum_{i<j} \mu_{i\alpha} \mu_{j\beta} T_{\alpha\beta}^{(2)}(r_{ij}) + \sum_i \frac{1}{2\alpha_i} |\mu_i|^2 \quad (5)$$

In the equation above, $T_{\alpha}^{(1)}$ is the charge-dipole interaction tensor, $T_{\alpha\beta}^{(2)}$ is the dipole-dipole interaction tensor, α_i is the polarizability of ion i , and μ_i is the set of dipoles, while $g_{ij}(r_{ij})$ is a damping function similar to Eq. (6):

$$g_{ij}(r_{ij}) = 1 - C_{ij} e^{-b_{ij} r_{ij}} \sum_{k=0}^4 \frac{(b_{ij} r_{ij})^k}{k!} \quad (6)$$

The parameters were derived in a semi-classical approach from ab initio calculations by Dewan [30] and validated by comparing the data from simulations with experimental data on the phase diagram, density, viscosity, electrical conductivity, thermal conductivity, and heat capacity [30]. For completeness they are listed in Table 2:

The systems were equilibrated for 500 ps in the NPT ensemble at 0 GPa and the corresponding temperature 50 K above the liquidus (Table 8), from which the equilibrium volume was taken. This was followed by a 100 ps equilibration and finally a 500 ps production run in the NVT ensemble at the same temperature. Time steps in all runs were set to 0.5 fs, while the relaxation time for both the Nosé-Hoover thermostat and barostat (for the NPT run) was set to 10 ps. The cubic simulation cell contained 600–800 ions in periodic boundary conditions. Cut-offs for the real space part of the Ewald sum and short-range potential were both set to half the length of the cell. Simulations at higher temperatures and different compositions were also performed; they are summarized in Table 3. In this case, the NPT run was 500 ps, and the NVT production run 500 ps to 2.5 ns.

4. Thermodynamic modelling

Optimizations of the thermodynamic model for the LiF-UF₄ system was done according to the CALPHAD (CALCulation of PHase Diagram) method [6] as implemented in the Factsage software [32]. To carry out such an optimization, the identity of the phases present in the system of interest must be known, as well as their respective Gibbs energy functions.

4.1. Pure compounds

The Gibbs energy function of a pure compound is given by:

$$G(T) = \Delta_f H_m^0(298) - S_m^0(298)T + \int_{298}^T C_{p,m}(T) dT - T \int_{298}^T \frac{C_{p,m}(T)}{T} dT \quad (7)$$

where $\Delta_f H_m^0(298)$ is the standard enthalpy of formation, $S_m^0(298)$ is the standard absolute entropy, both evaluated at a reference temperature, in this case 298.15 K (throughout this work 298 will be understood to mean 298.15 K for simplicity), and $C_{p,m}$ is the isobaric heat capacity expressed as a polynomial:

$$C_{p,m}(T) = a + bT + cT^2 + dT^{-2} \quad (8)$$

with more terms added if necessary.

In this work, the Neumann-Kopp rule [33] was used to approximate heat capacities of intermediate compounds in the absence of

Table 2
Parameter values for LiF-UF₄ PIM potential, with values in atomic units [30].

Ion pair	A _{ij}	a _{ij}	C _{ij} ⁶	C _{ij} ⁸	b _{ij} ⁶	b _{ij} ⁸	b _{ij} ^D	c _{ij} ^D
F ⁻ -F ⁻	282.3	2.440	15.0	150.0	1.9	1.9		
F ⁻ -U ⁴⁺	70.623	1.666	38.7	387.0	1.9	1.9	b _{FU} ^D = b _{UF} ^D = 1.7516	c _{UF} ^D = 1.8148
F ⁻ -Li ⁺	18.8	1.97	1.22	12.2	1.9	1.9	b _{FLi} ^D = 1.834	c _{FLi} ^D = 1.335
U ⁴⁺ -U ⁴⁺	1.0	5.0	100.0	1000.0	1.9	1.9		
U ⁴⁺ -Li ⁺	1.0	5.0	3.16	31.6	1.9	1.9	^b b _{ULi} ^D = 10.0	^b c _{ULi} ^D = 0.001
Li ⁺ -Li ⁺	1.0	5.0	0.10	1.0	1.9	1.9		

The polarizabilities of F⁻ and U⁴⁺ were set to 7.8935 au and 5.8537 au, respectively. Li⁺ is considered to be non-polarizable.

^aModified from c_{UF}^D = -0.84905 in Ref. [30].

^bNot defined in [30], set arbitrarily.

Table 3
Simulation conditions.

Composition / X(UF ₄)	N _{U⁴⁺}	N _{Li⁺}	N _{F⁻}	N _{total}	T / K	NPT / ns	NVT ^a / ns
0.25	72	216	504	792	831	0.5	0.5
0.50	114	114	570	798	1040	0.5	0.5
0.67	132	66	594	792	1216	0.5	0.5
0	400	400	800	900-1400 ^b		0.5	2.5
0.025	401	1	397	799	1121, 1400	0.5	0.5
0.104	36	310	454	800	900-1400 ^b	0.5	2.5
0.211	64	240	496	800	900-1400 ^b	0.5	2.5
0.296	82	195	523	800	900-1400 ^b	0.5	2.5
0.400	100	150	550	800	900-1400 ^b	0.5	2.5
0.513	116	110	574	800	900-1400 ^b	0.5	2.5
0.597	126	85	589	800	900-1400 ^b	0.5	2.5
0.715	138	55	607	800	900-1400 ^b	0.5	2.5
0.807	146	35	619	800	900-1400 ^b	0.5	2.5
0.911	154	15	631	800	900-1400 ^b	0.5	2.5
1	160	0	640	800	900-1400 ^b	0.5	2.5

^aNVT equilibration time was 0.2 ns in all cases.

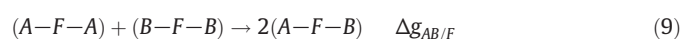
^bThe temperatures were: 900, 1000, 1121, 1300, and 1400 K wherever 900-1400 K is indicated.

experimental data. The thermodynamic data for all compounds in this study are listed in Table 4. The data for both solid and liquid LiF and UF₄ were taken from [17,34], respectively. The standard enthalpy of formation and standard entropy at 298.15 K of the intermediate compounds were optimized to closely match phase equilibrium data.

4.2. Liquid solution

All excess Gibbs energy terms of the liquid solution presented here have been modelled using an advanced modified quasi-chemical model akin to the one recently reported for the LiF-BeF₂ system [16]. The modified quasi-chemical model proposed by Pelton et al. [35] is particularly well adapted to describe ionic liquids such as in the present system, as it allows to select the composition of maximum short-range ordering (SRO) by varying the ratio between the cation-cation

coordination numbers Z^A_{AB/FF} and Z^B_{AB/FF} (fluorine is in this case the only anion present). The quadruplet approximation assumes a quadruplet, composed of two anions and two cations, to be the basic unit in liquid solution, and the excess parameters to be optimized are those related to the following second-nearest neighbor (SNN) exchange reaction:



where the fluoride anions are represented by F, and A and B denote the cations. Δg_{AB/F} is the Gibbs energy change associated with the SNN exchange reaction, and has the following form:

$$\Delta g_{AB/F} = \Delta g_{AB/F}^0 + \sum_{i \geq 1} g_{AB/F}^{i0} \chi_{AB/F}^i + \sum_{j \geq 1} g_{AB/F}^{0j} \chi_{BA/F}^j \quad (10)$$

where Δg⁰_{AB/F} and g^{ij}_{AB/F} are coefficients which may or may not be temperature-dependent, but which are independent of composition.

The dependence on composition is given by the χ_{AB/F} terms defined as:

$$\chi_{AB/F} = \frac{X_{AA}}{X_{AA} + X_{AB} + X_{BB}} \quad (11)$$

where X_{AA}, X_{BB} and X_{AB} represent cation-cation pair mole fractions.

The anion coordination number is finally fixed by conservation of charge in the quadruplet:

$$\frac{q_A}{Z_{AB/FF}^A} + \frac{q_B}{Z_{AB/FF}^B} = \frac{2q_F}{Z_{AB/FF}^F} \quad (12)$$

where q_i are the charges of the different ions, and Z^F_{AB/FF} is the anion-anion coordination number, in this case fluorine-fluorine.

Despite its usefulness, the thermodynamic model just outlined does not account for the formation of molecular species or heteropolyanions in the melt. As will be discussed at length in the following sections, (Li, U)F_x is not a solution in which cations and anions are completely dissociated. UF₄ is a Lewis acid and accepts fluoride anions from LiF, a Lewis

Table 4

Thermodynamic data for end-members and intermediate compounds used in this work for the phase diagram assessment: Δ_fH_m⁰(298 K)/(kJ·mol⁻¹), S_m⁰(298 K)/(J·K⁻¹·mol⁻¹), and heat capacity coefficients C_{p, m}(T/K)/(J·K⁻¹·mol⁻¹), where C_{p, m}(T/K) = a + b·T + c·T² + d·T⁻². Optimized data are shown in **bold**.

Compound	Δ _f H _m ⁰ (298 K)/	S _m ⁰ (298 K)/	C _{p, m} (T/K)/(J·K ⁻¹ ·mol ⁻¹) = a + b·T + c·T ² + d·T ⁻²				Reference
	(kJ·mol ⁻¹)	(J·K ⁻¹ ·mol ⁻¹)	a	b	c	d	
LiF(cr)	-616.931	35.66	43.309	1.6312·10 ⁻²	5.0470·10 ⁻⁷	-569,124	[17]
LiF(l)	-598.654	42.962	64.183				[17]
UF ₄ (cr)	-1914.200	151.7	114.5194	2.0555·10 ⁻²		-413,159	[34]
UF ₄ (l) ^a	-1914.658	115.4	174.74				[34]
Li₄UF₈(cr)	-4345.920	357.55	287.75532	8.5804·10 ⁻²	2.0188·10 ⁻⁶	-2,689,653	This work, [7]
Li₃UF₇(cr)	-3776.464	258.68	244.44634	6.9491·10 ⁻²	1.5141·10 ⁻⁶	-2,120,530	This work
LiUF₃(cr)	-2542.591	187.4	157.8284	3.6867·10 ⁻²	5.0470·10 ⁻⁷	-982,283	This work
LiU₄F₁₇(cr)	-8292.061	644.7	501.38658	9.8532·10 ⁻²	5.0470·10 ⁻⁷	-2,221,760	This work

^aUF₄(l) is modelled as a [U_{1/11}F₄(1) - U_{1/11}F₄(1) - U_{2/22}F₈(1)] mixture with g⁰_[U_{1/11}F₄(1)] = 1/2 g⁰_[U_{2/22}F₈(1)] + 150,000 J·mol⁻¹.

base. The solution, as UF₄ is added to LiF, is formed by discrete coordination complexes which link to each other as soon as their number density is high enough, forming dimers, trimers, and ‘polymers’ (see Fig. 10a, b). In order to capture this structural evolution and provide a more accurate description of the chemical speciation in the melt, a coupled structural-thermodynamic model comparable to the one recently reported for the LiF-BeF₂ system [16] was adopted. The key distinction made by Smith et al. [16], was to introduce quadruplets which not only include Be²⁺, but also Be₂⁴⁺, Be₃⁶⁺, assigning them coordination environments 4, 7, and 10, respectively. That is, the authors effectively included monomers, dimers, and trimers, choosing suitable compositions of maximum short-range ordering for each one. In this work, two distinct cations were taken into account, with coordination numbers 7 and 8 (which dominate the distribution of [UF_x]^{4-x} complexes as shown in Section 6.2.3), as well as a 14-coordinated cation (the most abundant according to MD simulations): U_[VII]⁴⁺, U_[VIII]⁴⁺, U_{2[XIV]}⁸⁺. The cation-cation coordination numbers, shown in Table 5, were chosen to reflect the compositions of maximum SRO in the neighborhood of X(UF₄) = 0.20 (Li₄UF₈), and X(UF₄) = 0.25 (Li₃UF₇, “Li₆U₂F₁₄”).

The choice of assigning every species with two or more bridged U⁴⁺ centers to the dimer distribution was motivated by the need to keep fitting parameters from being too numerous to have a practical model, while still retaining a rigorous structural description. In this regard, the need to reflect more than one coordination number in the first shell surrounding U⁴⁺, which is such a salient feature of the (Li,U)F_x melt, motivated the inclusion of two distinct monomers. Ultimately, pure UF₄(l) is modelled as a solution of dimers. To do so, the reactions $\frac{1}{2}U_{2[XIV]}F_8(l) = U_{[VII]}F_4(l)$ and $\frac{1}{2}U_{2[XIV]}F_8(l) = U_{[VIII]}F_4(l)$ were constrained by the following Gibbs energy expressions (respectively, Eq. 13, 14):

$$g_{U_{[VII]}F_4(l)}^0 = \frac{1}{2}g_{U_{2[XIV]}F_8(l)}^0 + 150000 J \cdot mol^{-1} \tag{13}$$

$$g_{U_{[VIII]}F_4(l)}^0 = \frac{1}{2}g_{U_{2[XIV]}F_8(l)}^0 + 150000 J \cdot mol^{-1} \tag{14}$$

The value of 150,000 J · mol⁻¹ is an arbitrary term to destabilize the monomers, insofar as it allows to reproduce the melting point (1307.8 K vs. (1307.9 ± 3.0) K [18]) and the enthalpy of fusion of UF₄ (45 kJ · mol⁻¹ vs. 46.986 kJ · mol⁻¹ [36]).

In the modified quasi-chemical model, interpolation to higher order systems is either symmetric or asymmetric, the choice depending on the similarity of the components between each other in a sublattice [37]. In the (Li,U)F_x solution, the uranium cations are taken to be symmetric with respect to each other, while the smaller, monovalent, non-polarizable Li⁺ is taken to be the asymmetric component. Thus, the virtual ternary systems {LiF + U_[VII]F₄ + U_[VIII]F₄}, {LiF + U_[VII]F₄ + U₂F₈}, and {LiF + U_[VIII]F₄ + U₂F₈} are asymmetric, while {U_[VII]F₄ + U_[VIII]F₄ + U₂F₈} is symmetric. Then for each quadruplet, the composition dependence (Eq. 11) expressed as a function of cation-cation pair mole fraction is:

Table 5
Cation-cation coordination numbers of the liquid solution.

A	B	Z _{AB,FF} ^A	Z _{AB,FF} ^B
Li ⁺	Li ⁺	6	6
U _[VII] ⁴⁺	U _[VII] ⁴⁺	6	6
U _[VIII] ⁴⁺	U _[VIII] ⁴⁺	6	6
U _{2[XIV]} ⁸⁺	U _{2[XIV]} ⁸⁺	6	6
U _[VII] ⁴⁺	U _[VIII] ⁴⁺	6	6
U _[VIII] ⁴⁺	U _[VII] ⁴⁺	6	6
U _[VII] ⁴⁺	U _{2[XIV]} ⁸⁺	6	6
U _[VIII] ⁴⁺	U _{2[XIV]} ⁸⁺	6	6
Li ⁺	U _[VII] ⁴⁺	2	6
Li ⁺	U _[VIII] ⁴⁺	1.5	6
Li ⁺	U _{2[XIV]} ⁸⁺	1	6

$$\chi_{LiU_{[VII]}/FF} = \chi_{LiU_{[VIII]}/FF} = \chi_{LiU_2/FF} = \frac{X_{LiLi}}{\sum_A \sum_B X_{AB/F_2}} \tag{15}$$

$$\chi_{U_{[VII]}Li/FF} = \chi_{U_{[VIII]}Li/FF} = \chi_{U_2Li/FF} = \frac{X_{U_{[VII]}U_{[VII]}} + X_{U_{[VIII]}U_{[VIII]}} + X_{U_2U_2} + X_{U_{[VII]}U_{[VIII]}} + X_{U_{[VII]}U_2} + X_{U_{[VIII]}U_2}}{\sum_A \sum_B X_{AB/F_2}}$$

Note that the denominator $\sum_A \sum_B X_{AB/F_2}$ adds to 1 in the {LiF + “UF₄”} system.

Having established the composition dependence, the optimized excess Gibbs energy parameters of the binary liquid solution in the LiF-UF₄ system are shown in Eq. 16–18. The parameters were optimized based on the complex anion distribution as calculated with MD (see Fig. 15a, b) and phase diagram equilibria points of the liquidus (see Fig. 14).

$$\Delta g_{LiU_{[VII]}/FF} = -59500 + (-2600 + 0.4 \cdot T) \chi_{LiU_{[VII]}/FF} J \cdot mol^{-1} \tag{16}$$

$$\Delta g_{LiU_{[VIII]}/FF} = -59500 + (-2600 - 0.3 \cdot T) \chi_{LiU_{[VIII]}/FF} J \cdot mol^{-1} \tag{17}$$

$$\Delta g_{LiU_{2[XIV]}/FF} = -32000 + (-1000 - 0.8 \cdot T) \chi_{LiU_{2[XIV]}/FF} - 26 \cdot T \chi_{U_{2[XIV]}Li/FF} J \cdot mol^{-1} \tag{18}$$

5. Brief review of literature data on the LiF-UF₄ system

Barton et al. [5] was the first to produce a sketch of the LiF-UF₄ phase diagram in 1958, shown in Fig. 1. The authors used a combination of i) thermal analysis, namely examination of cooling curves, ii) quenching of samples after equilibration, iii) differential thermal analysis, and iv) visual observation methods coupled with XRD. The authors identified three incongruently melting compounds: Li₄UF₈ (T_{peritectic} = 773 K), Li₇U₆F₃₁ (T_{peritectic} = 883 K), LiU₄F₁₇ (T_{peritectic} = 1048 K) and a single eutectic at T = 763 K, X(UF₄) = 0.27. The features of the diagram are summarized in Table 6. Besides the stable phases, a meta-stable, so-called “X-phase” was detected by them and hypothesized to be Li₃UF₇.

A few years later Weaver et al. [38] studied the LiF-ThF₄-UF₄ system and reported no ternary compounds but four solid solutions, amongst which was Li₃(Th,U)F₇. In 2010, the binary system was optimized by Beneš et al. [7] based on the experimental data from Barton et al. [5] using a modified quasi-chemical model in the quadruplet

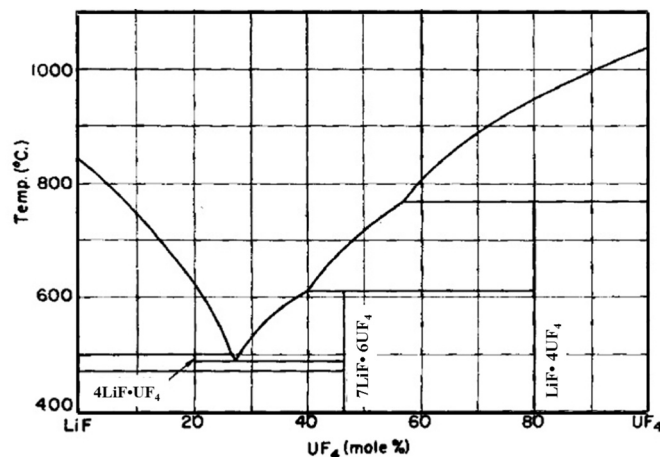


Fig. 1. The system LiF-UF₄ as reported by Barton et al. [5]. Reproduced with permission from Wiley and Sons.

Table 6
Invariant equilibria in the LiF-UF₄ system.

Equilibrium	Invariant reaction	This study (calc.)		DSC equilib. ^b		Barton et al. [5]	
		X(UF ₄)	T/K	X(UF ₄) ^a	T/K	X(UF ₄) ^c	T/K ^d
Eutectoid	Li ₄ UF ₈ = LiF + LiUF ₅	0.20	750	0.20	755 ± 2	0.20	743
Peritectic	Li ₄ UF ₈ = LiF + L	0.257	766	-	761 ± 1	0.26	773
Eutectic	L = Li ₄ UF ₈ + LiUF ₅	0.263	758	0.27	762 ± 4	0.27	763
Peritectic ^e	LiUF ₅ = LiU ₄ F ₁₇ + L	0.396	879	-	877 ± 7	0.4	883
Peritectic	LiU ₄ F ₁₇ = UF ₄ + L	0.568	1044	-	1044 ± 20	0.57	1048

^aStandard uncertainties u are u(X(UF₄)) = 0.05.^bGlobal average of the experimental runs appearing in Table 6.^cStandard uncertainty u reported by the authors: u(X(UF₄)) = 0.01.^dStandard uncertainty u reported by the authors: u(T) = 1 K.^eAuthors mention phase Li₇U₆F₃₁ instead of LiUF₅, see Section 6.1.3.^fMeasurements done at (0.10 ± 0.005) MPa.

approximation to describe the liquid solution. The optimization included Li₇U₆F₃₁ instead of LiUF₅ and did not consider Li₃UF₇ as a phase in the binary system, but did model the Li₃(Th,U)F₇ solid solution. Hereafter is a discussion of the findings in this work compared to the phase diagram as reported by Barton et al.

6. Results and discussion

6.1. Phase diagram studies in the LiF-UF₄ system

6.1.1. Li₄UF₈

Barton et al. [5] reported quite a narrow range of stability for Li₄UF₈, i.e. from 743 K to 773 K (Fig. 1). Our attempts to quench a pure sample of composition Li₄UF₈ were unsuccessful. Nevertheless, it was found in combination with LiUF₅ and UF₃ impurity in an attempt to isolate Li₃UF₇; Li₄UF₈ has orthorhombic symmetry and belongs to space group *Pnma* as identified by Brunton [39]. The diffractogram of this three-phase mixture with its LeBail refinement is shown in Fig. 2.

In another synthesis attempt, at composition X(UF₄) = 0.123 (diffractogram shown in Fig. 3), Li₄UF₈ was not observed anymore, in agreement with the phase equilibria reported by Barton et al. [5].

6.1.2. Li₃UF₇

Upon quenching samples with compositions ranging from X(UF₄) = 0.2 to 0.32 from above the solidus temperature, Barton et al. [5] observed a crystalline phase with a diffraction pattern they could

not match with the established phases in the system. The authors simply designated it as X-phase and concluded that it was metastable, since it formed only during certain cooling conditions. In particular, it formed when the mass of the samples was large, but not when optimal quenching conditions (small masses) were used. They suggested 3LiF·UF₄ to be the stoichiometry of the X-phase. As mentioned above, an attempt to synthesize the Li₃UF₇ phase in this work resulted in the quenching of the high temperature phase Li₄UF₈ along with LiUF₅, as well as a UF₃ impurity, probably due to reduction from the nickel liner. Yet in an attempt to ascertain whether or not Li₄UF₈ is stable down to room temperature, LiUF₅ could be identified as expected, but interestingly, the other crystalline phase belonged to the same space group as one of the known phases of Li₃ThF₇ [40], *P4/ncc* (Fig. 3). Thus the hypothesis that Li₃UF₇ was the identity of the X-phase appears to be correct, as well as its metastability given the absence of the line compound at the composition where it should have formed, X(UF₄) = 0.25 (Fig. 2).

6.1.3. LiUF₅

Barton et al. [5] reported the line compound Li₇U₆F₃₁ to be stable, guessing the stoichiometry based on the existence of Na₇U₆F₃₁ and K₇U₆F₃₁. Discrepancies between the density obtained from the mass of two formula units and the proposed cell parameters [41], and that obtained from measurements raised doubts about the validity of the 7:6 stoichiometry, however. The mismatch between the crystal system and space group of the putative phase Li₇U₆F₃₁ (tetragonal, *I4₁/a*) and

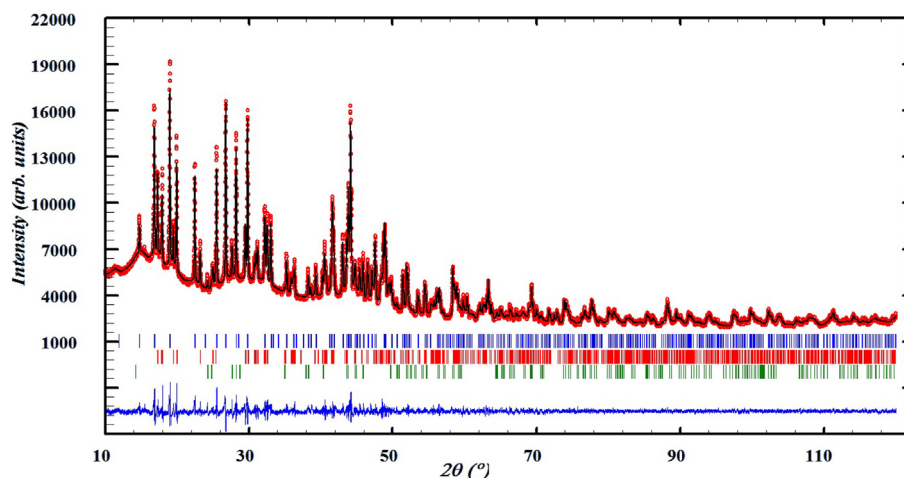


Fig. 2. Diffractogram of the LiUF₅-Li₄UF₈ mixture, X(UF₄) = 0.25. Comparison between the observed (Y_{obs} , in red) and calculated (Y_{calc} , in black) X-ray diffraction patterns. $Y_{obs} - Y_{calc}$, in blue, is the difference between the experimental and calculated intensities. The Bragg's reflection angular positions are marked in blue (LiUF₅), red (Li₄UF₈), and green (UF₃).

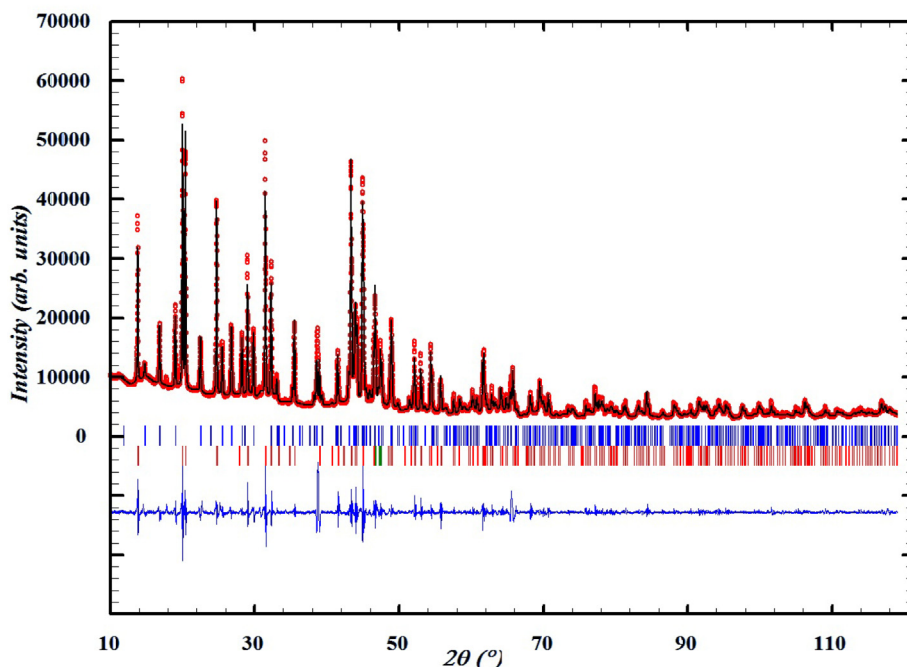


Fig. 3. Diffractogram of the LiUF₅-Li₃UF₇ mixture, X(UF₄) = 0.123. Comparison between the observed (Y_{obs} , in red) and calculated (Y_{calc} , in black) X-ray diffraction patterns. $Y_{obs} - Y_{calc}$, in blue, is the difference between the experimental and calculated intensities. The Bragg's reflection angular positions are marked in blue (LiUF₅), and red (Li₃UF₇).

A₇U₆F₃₁ (A = Na, K) (trigonal, $R\bar{3}$) raised further concerns. Addressing these doubts, Brunton [42] later showed that the correct formula is LiUF₅. More recently Yeon et al. also grew LiUF₅ crystals in a hydrothermal environment [43]. In this work, a sample of high purity LiUF₅ (space group $I4_1/a$) could be crystallized from a melt with composition X(UF₄) = 0.5 (Fig. 4). LiUF₅ was thus included in the thermodynamic model and it is recommended that molten salt databases use this compound rather than Li₇U₆F₃₁.

6.1.4. LiU₄F₁₇

No crystal structure determination could be found in the literature for either LiU₄F₁₇ or LiTh₄F₁₇, and there were no thermal-analysis data collected by Barton et al. [5] in the vicinity of X(UF₄) = 0.8. However, the calorimetric measurements reported in the LiF-ThF₄ system [11] support the existence of such a phase, as do the DSC data collected in this work, listed in Table 6. Furthermore, Cousson and Pages [44] were able to prepare crystals of LiAn₄F₁₇ (An = Th, U), of tetragonal

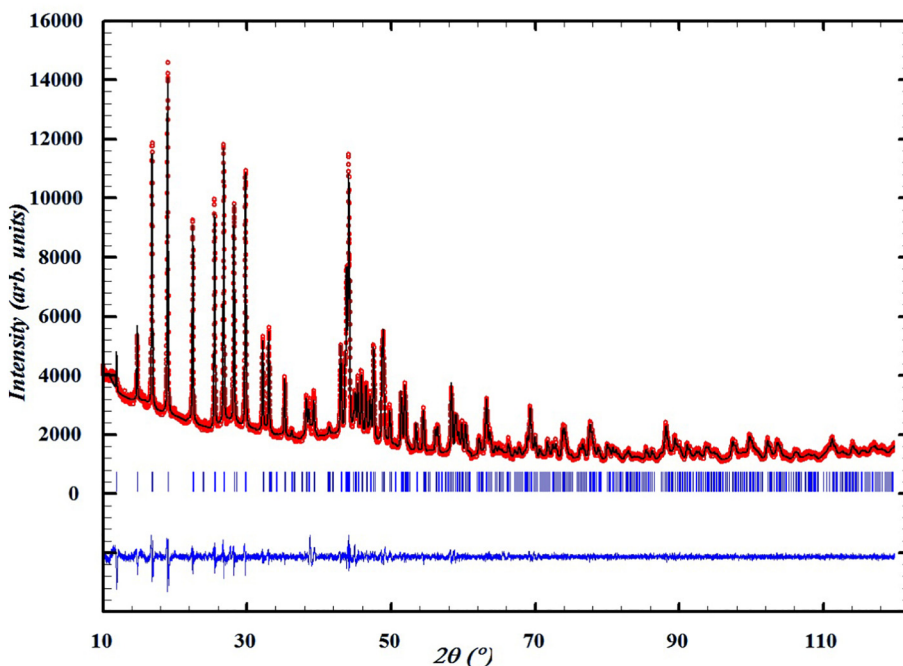


Fig. 4. Diffractogram of LiUF₅, X(UF₄) = 0.5. Comparison between the observed (Y_{obs} , in red) and calculated (Y_{calc} , in black) X-ray diffraction patterns. $Y_{obs} - Y_{calc}$, in blue, is the difference between the experimental and calculated intensities. The Bragg's reflection angular positions are marked in blue.

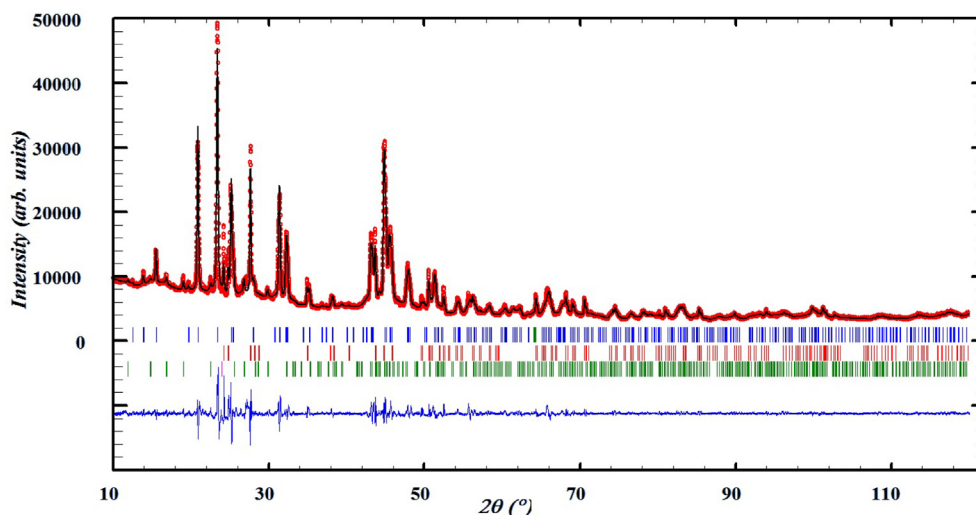


Fig. 5. XRD pattern of a sample with composition $X(\text{UF}_4) = 0.8$. Three phases contribute to the pattern: LiUF_5 (Bragg's reflection angular position marked in blue), $\text{LiU}_4\text{F}_{17}$ (red), and UF_3 (green). Comparison between the observed (Y_{obs} , in red) and calculated (Y_{calc} , in black) X-ray diffraction patterns. $Y_{\text{obs}} - Y_{\text{calc}}$, in blue, is the difference between the experimental and calculated intensities.

Table 7
Equilibrium data in the $\text{LiF}-\text{UF}_4$ system as measured in this work by DSC.

$X(\text{UF}_4)^a$	T/K ^b	Equilibrium	Equilibrium reaction
0.000	1118	LiF congruent melting	$\text{LiF} = \text{L}$
0.094	753	Eutectoid	$\text{Li}_4\text{UF}_8 = \text{LiF} + \text{LiUF}_5$
0.094	761	Peritectic	$\text{Li}_4\text{UF}_8 = \text{LiF} + \text{L}'$
0.094	1074	Liquidus	$\text{LiF} + \text{L}' = \text{L}$
0.2	756	Eutectoid	$\text{Li}_4\text{UF}_8 = \text{LiF} + \text{LiUF}_5$
0.2	762	Peritectic	$\text{Li}_4\text{UF}_8 = \text{LiF} + \text{L}'$
0.27	770	Eutectic	$\text{Li}_4\text{UF}_8 + \text{LiUF}_5 = \text{L}$
0.329	762	Eutectic	$\text{Li}_4\text{UF}_8 = \text{LiF} + \text{LiUF}_5$
0.329	830	Liquidus	$\text{LiUF}_5 + \text{L}' = \text{L}$
0.399	760	Eutectic	$\text{Li}_4\text{UF}_8 = \text{LiF} + \text{LiUF}_5$
0.399	881	Peritectic	$\text{LiUF}_5 = \text{L} + \text{LiU}_4\text{F}_{17}$
0.445	761	Eutectoid	$\text{Li}_4\text{UF}_8 = \text{LiF} + \text{LiUF}_5$
0.445	878	Peritectic	$\text{LiUF}_5 = \text{L} + \text{LiU}_4\text{F}_{17}$
0.499	759	Eutectic	$\text{L} = \text{LiUF}_5 + \text{Li}_4\text{UF}_8$
0.499	882	Peritectic	$\text{LiUF}_5 = \text{L} + \text{LiU}_4\text{F}_{17}$
0.499	1060	Liquidus	$\text{L}' + \text{LiU}_4\text{F}_{17} = \text{L}$
0.602	758	Unknown	-
0.602	875	Peritectic	$\text{LiUF}_5 = \text{L} + \text{LiU}_4\text{F}_{17}$
0.602	1026	Peritectic	$\text{LiU}_4\text{F}_{17} = \text{UF}_4 + \text{L}$
0.642	872	Peritectic	$\text{LiUF}_5 = \text{L} + \text{LiU}_4\text{F}_{17}$
0.642	1092	Liquidus	$\text{UF}_4 + \text{L}' = \text{L}$
0.717	867	Peritectic	$\text{LiUF}_5 = \text{L} + \text{LiU}_4\text{F}_{17}$
0.717	1095	Liquidus	$\text{UF}_4 + \text{L}' = \text{L}$
0.804	1057	Peritectic	$\text{LiU}_4\text{F}_{17} = \text{UF}_4 + \text{L}$
0.804	1222	Liquidus	$\text{UF}_4 + \text{L}' = \text{L}$
0.876	1031	Peritectic	$\text{LiU}_4\text{F}_{17} = \text{UF}_4 + \text{L}$
0.876	1263	Liquidus	$\text{UF}_4 + \text{L}' = \text{L}$
1.000	1306	Congruent melting	$\text{UF}_4 = \text{L}$

^aStandard uncertainties u are $u(X(\text{UF}_4)) = 0.005$.

^bStandard uncertainties u are $u(T) = 5$ K for the pure end-members, $u(T) = 10$ K for mixtures.

The pressure was (0.10 ± 0.005) MPa.

symmetry, and narrowed down the possible space groups of the compounds to three: $I4/m$, $I4$, or $I\bar{4}$. Unfortunately $\text{LiU}_4\text{F}_{17}$ could not be isolated as a pure phase material in the present work, but a sample with composition $X(\text{UF}_4) = 0.80$ yielded a phase which could not be attributed to either LiUF_5 (which also precipitated in the sample), or UF_4 , as would be the case if $\text{LiU}_4\text{F}_{17}$ did not exist. With the aid of a LeBail refinement, it could be established that amongst the space groups suggested by Cousson and Pages, $I4$ is the most likely one, as it resulted in the

best fit to the data, shown in Fig. 5. Note that there is a third phase in the refinement, again identified as UF_3 .

6.1.5. DSC measurements

The equilibria data in $\text{LiF}-\text{UF}_4$ were investigated in this work with DSC, with good agreement with the equilibria reported by Barton et al. [5]. The invariant equilibria as reported by the authors is compared to those calculated and measured in the present work, Table 6. The calorimetric measurements are presented in Table 7, and overlaid with the calculated phase diagram in Fig. 14 (▲, red).

6.2. Local structure of the $(\text{Li,U})\text{F}_x$ melt

6.2.1. EXAFS spectra and characterization of the local structures

The local structure characteristics of molten $(\text{Li,U})\text{F}_x$ salt were studied as a function of composition with three samples with increasing UF_4 content: $X(\text{UF}_4) = 0.25, 0.50, 0.67$. Their $k^2\chi(k)$ spectra are shown in Figs. 6a-8a, accompanied by the corresponding Fourier transform moduli in Figs. 6b-8b. In all figures the experimental data are compared with the results obtained from our MD simulations (red). These were computed by using the Cartesian coordinates of the ions in the NVT production runs as input for the FEFF8.40 code [45] and averaging over ~25,000 configurations. The resulting EXAFS signal could then be directly compared to the experimental one. Additionally, fits were calculated using the standard EXAFS Eq. [46] without cumulants (blue). Four parameters were refined during the fitting process with the standard EXAFS equation: the energy shift from the L_3 edge (ΔE_0), Debye-Waller factor (σ^2), the expected U-F distance $E[\text{R}_{\text{U-F}}]$, and the coordination number (CN). They are listed in Table 8.

Even though fitting of the EXAFS equation is routinely applied to liquid systems, it assumes a Gaussian distribution of interionic distances between equivalent neighbors and the absorbing central atom which does not reflect distributions in actual liquids, especially at high temperatures, where thermal disorder and anharmonicity start to play a major role [47]. The actual radial distribution functions (denoted as $g(r)$ or RDF) can, for instance, be obtained from neutron diffraction data or tallied from a large number of observations so as to capture thermal disorder and anharmonicity, as in MD. An example, at the composition $X(\text{UF}_4) = 0.25$, is shown in Fig. 9, where two peaks corresponding to the first two U-F coordination shells are shown. A fluoride ion can be

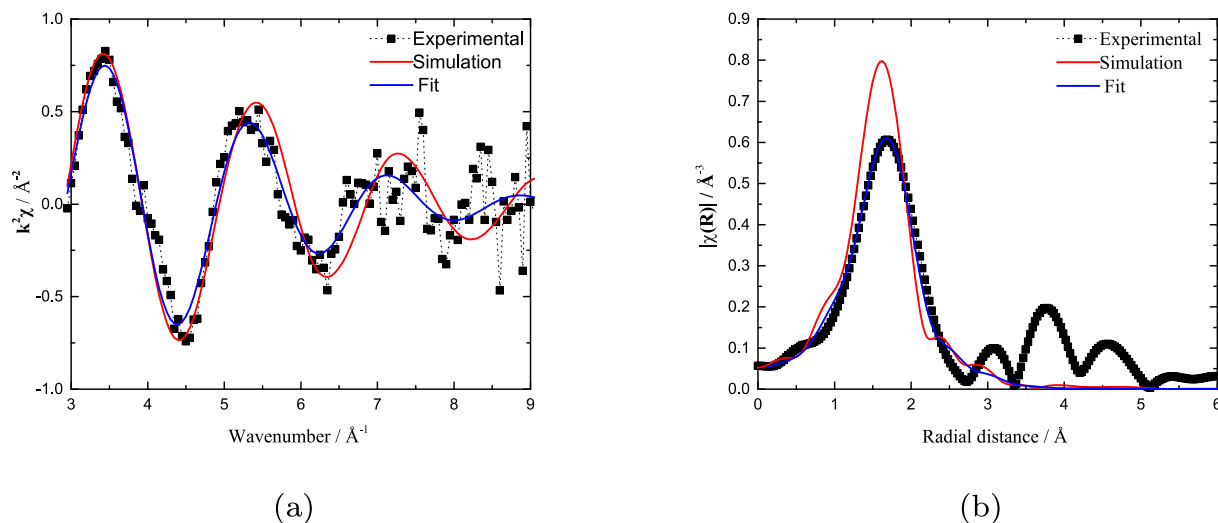


Fig. 6. (a) Experimental (■), simulated (red), and fitted (blue) $k^2\chi(k)$ spectra (collected in fluorescence mode) of a sample with composition $X(\text{UF}_4) = 0.25$ at $T = 831$ K. (b) Fourier transform modulus $|\chi(R)|$ of the EXAFS spectra.

defined to belong to the first coordination shell of U^{4+} when the U—F distance is less than R_{cutoff} , i.e. the first minimum of the U—F RDF (marked by the red line). The peak is skewed to the right, such that the most probable distance (maximum of the first peak) and expected bond length within the first shell, given by:

$$E[R^{U-F}] = \frac{\int_0^{R_{\text{cutoff}}} r_{U-F} \cdot g_{U-F}(r) dr}{\int_0^{R_{\text{cutoff}}} g_{U-F}(r) dr} \quad (19)$$

although close, do not coincide, a feature which cannot possibly be captured by a Gaussian distribution. Notwithstanding, it can be seen that the tail on the right is thin and comes close to zero, such that the peak can be reasonably approximated by a bell curve. In contrast, the same is not true for the second peak visible in the RDF, which has a fat tail on the right, and a bell curve would surely make a poor fit of it. For that reason, the fits included here are only for the first coordination shell, and are intended as an approximation to gauge the MD results.

6.2.2. Structural characteristics of the first coordination shell

The evolution of the average coordination around U^{4+} and the U—F interionic distance obtained by both methods is listed in Table 8. As already mentioned, an illustration of the tabulated most probable, expected, and bond cutoff lengths of the MD simulations is shown in Fig. 9. The agreement between both sets of data is good. The coordination number distribution which can be derived from the MD simulations (listed in Table 10) is dominated by 7, 8, and 9-coordinated U^{4+} , resulting in an average coordination between 7 and 8. This is consistent with the coordination environment of U(IV) fluorocomplexes in the solid state [48] as well as the 7 and 8-coordinations which have been observed by absorption spectroscopy in U(IV)-containing FLiNaK and FLiBE melts by Toth [49]. Most recently, molten-state EXAFS studies on LiF- UF_4 mixtures in the 5 to 30 mol% UF_4 range confirmed the coexistence of $[\text{UF}_7]^{3-}$ with $[\text{UF}_8]^{4-}$ and $[\text{UF}_9]^{5-}$ [50], which also result in an average CN between 7 and 8 (Table 8).

As for bond lengths, Bessada et al. [50] studied the average U—F distances as a function of the coordination number using MD simulations

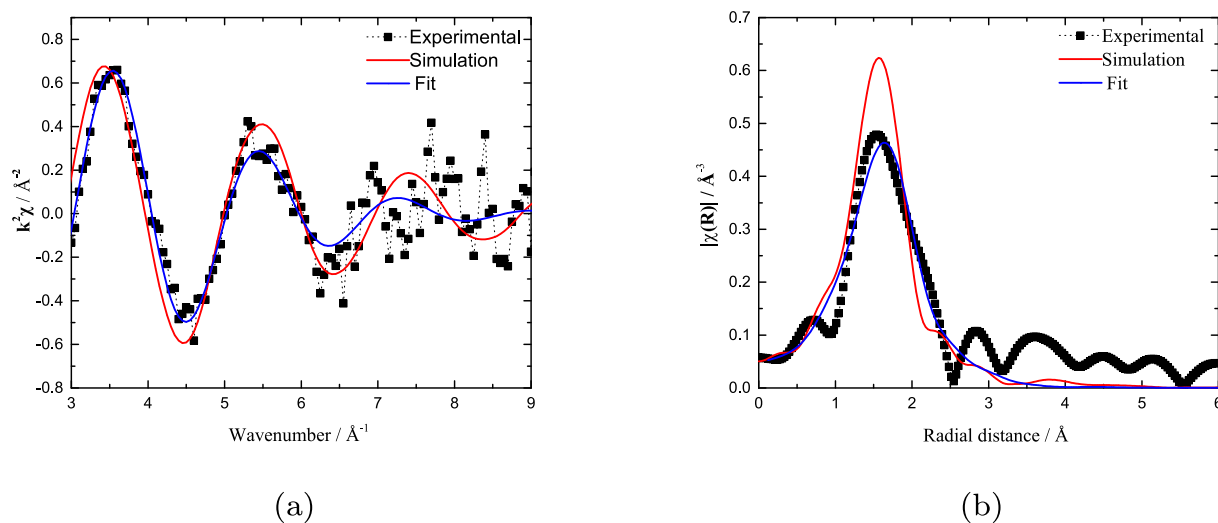


Fig. 7. (a) Experimental (■), simulated (red), and fitted (blue) $k^2\chi(k)$ spectra (collected in fluorescence mode) of a sample with composition $X(\text{UF}_4) = 0.50$ at $T = 1040$ K. (b) Fourier transform modulus $|\chi(R)|$ of the EXAFS spectra.

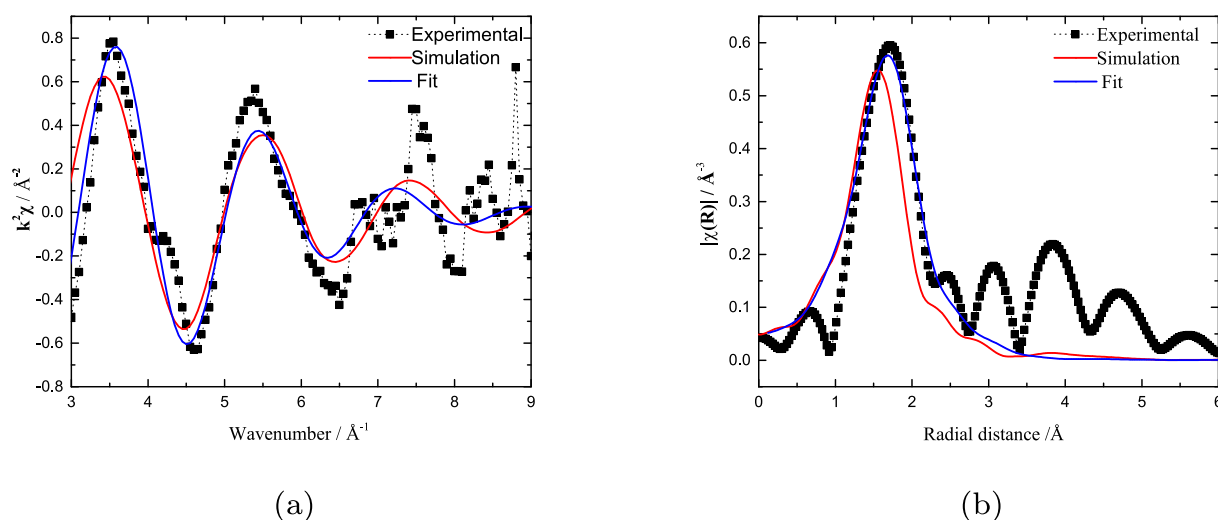


Fig. 8. (a) Experimental (■), simulated (red), and fitted (blue) $k^2\chi(k)$ spectra (collected in transmission mode) of a sample with composition $X(\text{UF}_4) = 0.67$ at $T = 1216$ K. (b) Fourier transform modulus $|\chi(R)|$ of the EXAFS spectra.

Table 8

Structural information of the first fluoride coordination shell around U^{4+} in the $(\text{Li,U})\text{F}_x$ solution as calculated in this work, 50 K above the liquidus line, compared to data by Bessada et al. [50] and Ocadiz-Flores et al. [51]. CN is the coordination number, σ^2 is the Debye-Waller factor, ΔE is the energy shift from the L_3 edge, R_f is the goodness of fit. Standard deviations are given in parentheses.

X(UF ₄)	Coordination number		Bond length				EXAFS fitting			T / K	Source
	CN _{U-F}	CN _{U-F}	R _{U-F} ^a	R _{U-F} ^b	E[R _{U-F}] ^c	E[R _{U-F}] ^b	ΔE	σ ²	R _f		
	MD	Fit	MD / Å	MD / Å	MD / Å	Fit / Å	Fit / eV	Fit / Å ²	Fit		
0.05	7.75				2.29					1175	[50]
0.10	7.68				2.28					1125	[50]
0.15	7.82				2.29					1075	[50]
0.20	7.86				2.29					1000	[50]
0.25	7.92	8.0(6)	2.18	3.00	2.26	2.26(1)	2.70(52)	0.021(1)	0.012	831	This work
0.274	7.90				2.29					825	[50]
	7.91				2.29					875	[50]
	7.85				2.29					925	[50]
	7.86				2.29					975	[50]
0.30	7.89				2.29				875	[50]	
0.5	7.80	7.6(7)	2.16	3.05	2.27	2.23(1)	1.24(8)	0.025(2)	0.004	1040	This work
0.67	7.72	7.7(8)	2.16	3.03	2.27	2.25(1)	4.14(92)	0.022(2)	0.039	1216	This work
	7.94	8.0(7)	2.21	3.06	2.28	2.27(1)	3.52(71)	0.030(2)	0.031	1357	[51]

^aMost probable distance, ^bbond cut-off = maximum U–F distance, ^cexpected value (Eq. 19). Fig. 9 illustrates how these distances differ.

and found averages of 2.17–2.18 Å, 2.23–2.24 Å, 2.29–2.30 Å, 2.35–2.38 Å, and 2.42–2.46 Å in the case of CN = 6, 7, 8, 9, and 10, respectively. The global averages found by the authors are listed in Table 8. They are rather insensitive to temperature and composition. The expected U–F distances according to the simulations in this work and in a related manuscript [51] (2.26–2.28 Å) are in good agreement with those of Bessada et al. (2.28–2.29 Å) and the standard fits (2.23–2.27 Å). From the Fourier transform moduli of the EXAFS data at compositions $X(\text{UF}_4) = 0.25$ and 0.67, it seems that the most probable bond length is slightly underestimated in the MD calculations. In general, the polarizability of species, and thus the potential itself, can change as a function of composition [52], and this underestimation could perhaps be corrected by adjusting the polarizability for every composition. Nevertheless, given the thorough validation of the potential by Dewan [30], and the good results it has also produced with the EXAFS spectra collected by Bessada et al. [50], the results are satisfactory.

It is also instructive to compare with simulations of LiF–ThF₄ melts at several compositions [14,25,50,53,54]. The results of these different authors are summarized in Table 9. Even if the most probable actinide-fluoride distance is very similar in both binary systems, the actinide contraction effect is evident in the bond cutoff distances, as $\max[R_{U-F}] < \max[R_{Th-F}]$ at all compositions. Similarly one can observe that, $E[R_{U-F}] < E[R_{Th-F}]$.

Another interesting feature is that the average U–F distance either shortens or remains the same in molten $(\text{Li,U})\text{F}_x$ when compared to the distance in the known solid phases (see Section 6.1): 2.34(11)¹ Å in LiUF₅, 2.29(6)² Å in Li₄UF₈ and 2.28(2)³ Å in UF₄. Dai et al. [54] observed a similar Th–F shortening in molten ThF₄ compared to ThF₄ (cr), although the authors incorrectly interpreted it as an expansion of

¹ Averaged from the crystallographic data in [43].

² Averaged from the crystallographic data in [39].

³ Averaged from the crystallographic data in [55].

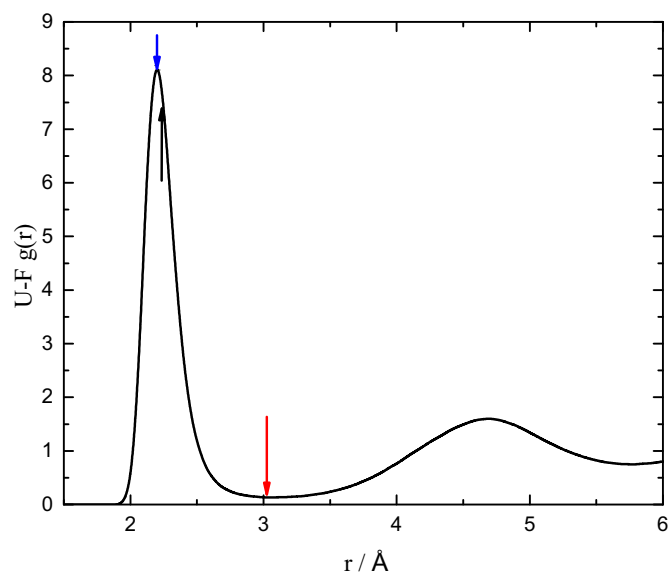


Fig. 9. Example of a U–F radial distribution function, $X(\text{UF}_4) = 0.25$. From left to right, the arrows indicate the position of the most probable, expected, and bond cutoff lengths.

Table 9

Summarized Th–F first neighbor distances as extracted from MD simulations of the $(\text{Li}, \text{Th})\text{F}_x$ melt by different authors.

$X(\text{ThF}_4)$	$R_{\text{Th-F}}^a / \text{Å}$	$E[R_{\text{Th-F}}^b] / \text{Å}$	$R_{\text{Th-F}}^c$	T / K	Reference
0.15		2.35		850	[50]
0.20		2.34		850	[50]
0.22	2.3		3.4	850	[14]
0.25		2.34		850	[50]
0.30		2.35		850	[50]
0.35		2.36		850	[50]
0.5	2.23		3.2	1193	[25]
0.67^d	2.24		3.2	1200	[53]
	2.215		3.1	1633	[54]

^aMost probable distance, ^bexpected value (Eq. 19), ^cbond cut-off = maximum Th–F distance.

Fig. 9 illustrates how these distances differ.

^dOther compositions were studied as well by the authors, but the maximum of the RDF was found to be insensitive to the ThF_4 concentration.

Table 10

Isothermal coordination number distribution and average or expected value of CN ($E[\text{CN}]$) of the $(\text{Li}, \text{U})\text{F}_x$ melts at $T = 1400$ K.

Composition	6 CN		7 CN		8 CN		9 CN		10 CN		$E[\text{CN}]$
	%	%	%	%	%	%	%	%	%		
0.025	4.4	42.4	48.2	4.9	0.1	7.54					7.54
0.104	5.5	46.0	43.5	4.9	0.1	7.48					7.48
0.211	10.0	49.3	36.3	4.3	0.1	7.35					7.35
0.296	10.0	46.1	37.6	6.0	0.2	7.40					7.40
0.400	11.5	45.3	36.3	6.6	0.3	7.39					7.39
0.513	9.5	41.9	39.4	8.7	0.5	7.49					7.49
0.597	8.6	40.4	40.8	9.6	0.6	7.53					7.53
0.715	5.9	35.5	44.9	12.9	0.9	7.67					7.67
0.807	5.9	35.7	44.8	12.7	0.8	7.67					7.67
0.911	4.1	31.4	47.7	15.6	1.2	7.78					7.78
1	3.0	28.1	49.7	17.8	1.4	7.86					7.86

the Th^{4+} coordination cage upon melting. This was because they incorrectly identified a shorter bond length of 2.087 Å as the average Th–F distance in $\text{ThF}_4(\text{cr})$ when in fact this distance corresponds to $\text{ThF}_4(\text{g})$ [56]. Liu et al. [53] identified a strengthening of the local structure

Table 11

Isothermal speciation distribution and expected value of CN of the $(\text{Li}, \text{U})\text{F}_x$ melt at $T = 1400$ K.

Composition	Fraction					
	$X(\text{UF}_4)$	$^a[\text{UF}_7]^{3-}$	$[\text{UF}_8]^{4-}$	$^b[\text{UF}_9]^{5-}$	$^c[\text{U}_2\text{F}_x]^{8-x}$	$^d[\text{U}_3\text{F}_y]^{12-y}$
0.025	0.468	0.482	0.050	0.00	0.00	0.00
0.104	0.317	0.268	0.030	0.239	0.027	0.118
0.211	0.143	0.087	0.011	0.160	0.116	0.483
0.296	0.037	0.025	0.004	0.039	0.027	0.867
0.40	0.007	0.005	0.001	0.004	0.002	0.981
0.513	0.0	0.0	0.0	0.0	0.0	1.0

^a The tails of the monomer distribution with lower CN have been added to CN = 7.

^b The tails of the monomer distribution with higher CN have been added to CN = 9.

^c The dominant dimer is $[\text{U}_2\text{F}_{14}]^{6-}$.

^d The dominant trimer is $[\text{U}_3\text{F}_{19}]^{7-}$.

upon melting by comparing the bond length in their MD simulations with a sum of the Th^{4+} and F^- crystal radii as tabulated by Shannon [57]: $r_{\text{Th-F}} = 2.36$ Å. Again, a better approach would be to look at the average distances in $\text{ThF}_4(\text{cr})$ as measured experimentally: 2.30(1)⁴ Å, 2.324(19)⁵ Å, and 2.32(3)⁶ Å. In the aforementioned bonding analysis per CN done by Bessada et al. [50], it is clear that this strengthening of the local structure is allowed by the reduced repulsion between fluorides in the first shell as the CN decreases, and so it does from solid to liquid. Experimental [58,59] and computational [60–63] results on alkali halides reveal the same behavior. A decreased shielding of the 2nd shell, which expands and becomes less populated, could also contribute to these changes in interionic distances [63].

6.2.3. Medium-range ordering

In addition to providing information on the coordination environment of the U species, the MD simulations have the benefit of giving detailed information on the medium-range structure. Two uranium ions are considered fluoride-bridged when the distance between them is less than $2 \cdot R_{\text{U-F, cutoff}}$ and less than the first minimum in the U–U RDF. As the UF_4 concentration increases, the number of fluoride bridges increases as well. The bridges identified consisted of 1 F^- (corner-sharing), 2 F^- (edge-sharing), or 3 F^- (face-sharing), with corner-sharing being the dominant bridging mechanism. Dimers and trimers start to appear until a ‘polymerized network’ is formed, in which all the U cations are connected by bridging fluorides. This evolution is shown in Table 11 and plotted at 1121 K and 1400 K in Fig. 10a, b. The concentration of both isolated coordination complexes and dimers decrease monotonically while the fraction of polymerized species rapidly increases; trimers reach a maximum at around $X(\text{UF}_4) = 0.2$, accounting for less than 20% of the species. The speciation is quite insensitive to temperature, with the polymer fraction increasing only slightly slower with UF_4 addition at $T = 1400$ K.

Network-like behavior has also been observed in MD simulations of LiF-BeF_2 [15], LiF-ZrF_4 [29], LiF-ThF_4 [53,54], $\text{LiF-BeF}_2\text{-ThF}_4$ [53], and $\text{LiF-ThF}_4\text{-UF}_4$ [50]. From the cage-out correlation function computed in some of those studies, it seems that the fragility of the coordination environments (as measured by their lifetimes) from lowest to highest is $\text{LiF-BeF}_2 > \text{LiF-ZrF}_4 > \text{LiF-ThF}_4$. This has implications on the properties at the macroscopic scale, e.g. the viscosity can change around 7 orders of magnitude from LiF to BeF_2 at a given temperature [64], while it only varies around one order of magnitude from LiF to ThF_4 [65], as it does from LiF to UF_4 [66]. Molten LiF-UF_4 is thus expected to have a similar fragility to LiF-ThF_4 , as characterized by the cage-out correlation function.

The solution remains saturated with ‘polymer’ beyond $X(\text{UF}_4) = 0.513$, see Fig. 10b.

⁴ From EXAFS data, [25].

⁵ From neutron diffraction data, [25]

⁶ Averaged from the crystallographic data in [55].

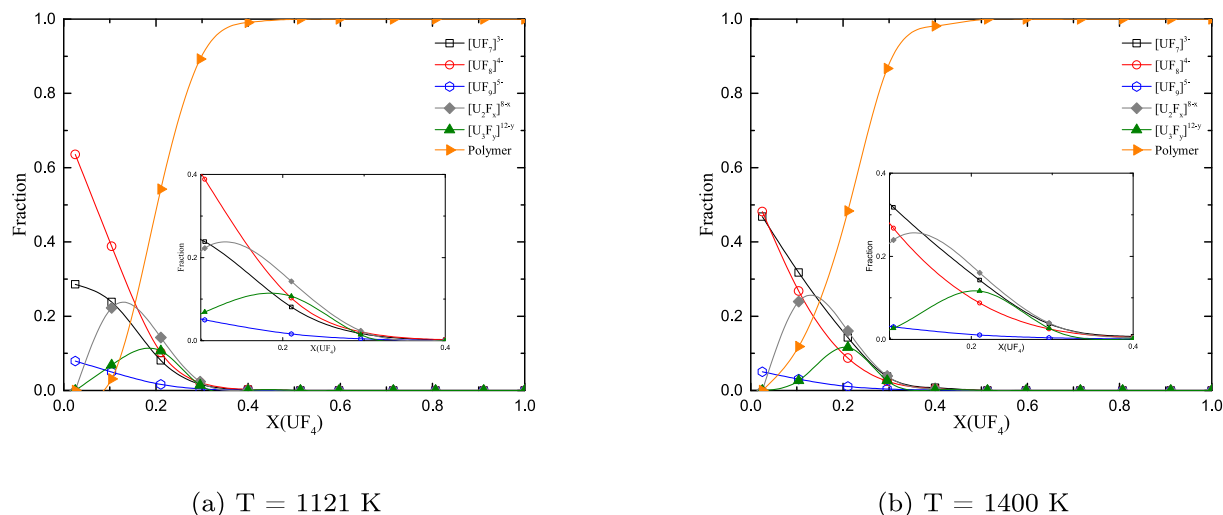


Fig. 10. Fraction of species in the (Li,U)F_x solution as a function of UF₄ mole fraction. The monomer contribution is split into the complex anions [UF₇]³⁻ (□, black), [UF₈]⁴⁺ (○, red), [UF₉]⁵⁻ (○, blue). Dimers indicated by: ♦, gray; trimers: ▲, green; chains with more than three U⁴⁺ centers are counted as 'polymers' (▶, orange). (a) T = 1123 K, (b) T = 1400 K. The inset is a zoom of the X(UF₄) = [0,0.4] interval, showing only the evolution of monomer, dimer and trimer. The values at T = 1400 K are listed in Table 11.

6.3. Excess properties of the (Li,U)F_x liquid solution

6.3.1. Excess density and molar volume

Relating the excess properties of molten salts to their structural properties is one of the motivations of the present work. Fig. 11a shows the comparison between density isotherms interpolated from the fitting equations to experimental data, given by Klimentkov et al. [67], and those calculated via MD in this work, in the 1000–1400 K range (in some cases the densities are extrapolated beyond the experimentally measured range). Superposed to these data are the experimental points by Blanke et al. [68] and Porter and Meaker [69], both at 1073 K. The agreement is quite good, with a slight overestimation of the density of pure UF₄(l). The inset in Fig. 11a shows the relative excess molar volume, i.e. $(V_{m, real} - V_{m, ideal})/V_{m, ideal}$, calculated from the density data shown in Fig. 11a. The volumes of the end-members to compute the ideal volume of mixtures was calculated from the equations of Klimentkov et al. for the three studies in the literature.

The MD predicts a positive excess of the molar volume, growing with increasing temperature, except in a very limited region at very high LiF content for the supercooled liquid at 1000 K. The excess deduced from Porter and Meaker [69] is also negative at high LiF content, while that from Blanke et al. [68] is positive throughout the reported compositions. In both cases the linear dependences of real molar volumes with composition (not shown) indicate that the behavior is not far from ideality [34]. Finally, the excess from Klimentkov et al. [67] is mostly positive except at high UF₄ content in the case of undercooled solution at T = 1000, 1121 K. As pointed out by the authors, positive deviations from ideality indicate interaction of the components, and they attributed the maximum in the 20 to 30 mol% region (for an isotherm they examined at 1270 K) to the formation of stable [UF₇]³⁻ complexes. As was discussed before (Section 6.2), the first coordination shell may even contract upon melting, so it does not contribute to free volume. Instead, the 2nd (and higher order) shells expand and have more voids, i.e., coordination complexes are farther apart from each other in the liquid than in the solid, and even more so in the mixtures than in the pure liquids, as the

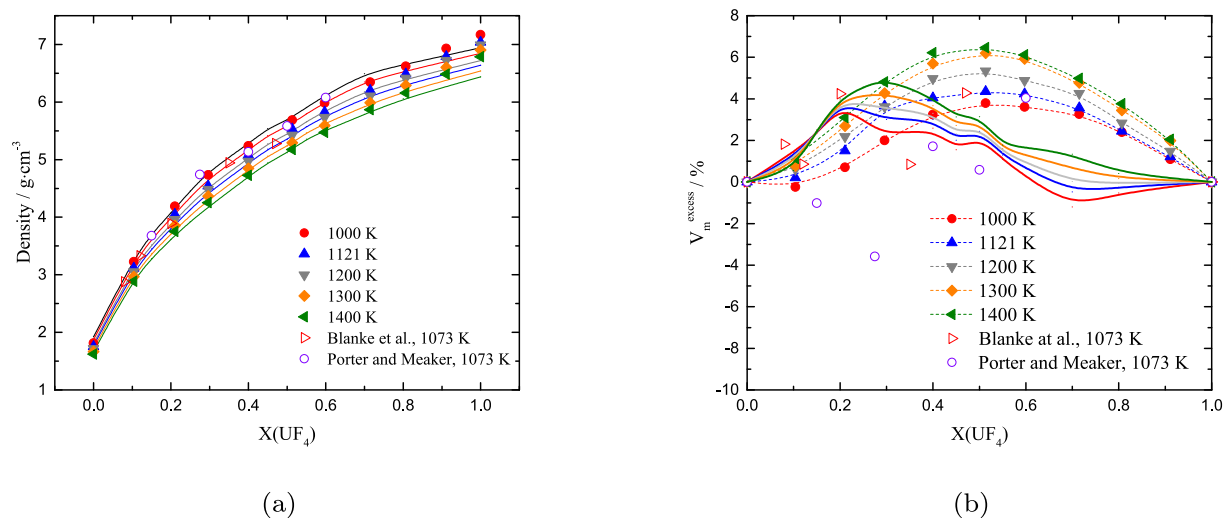


Fig. 11. Evolution of density. (a) Solid lines: isotherms calculated from the empirical equations reported by Klimentkov et al. [67]; solid symbols: results derived from MD simulations; ▶, red, experimental data by Blanke et al. [68] and ○ (purple) by Porter and Meaker [69], T = 1073 K. (b) Relative excess molar volume (%), of the (Li,U)F_x solution.

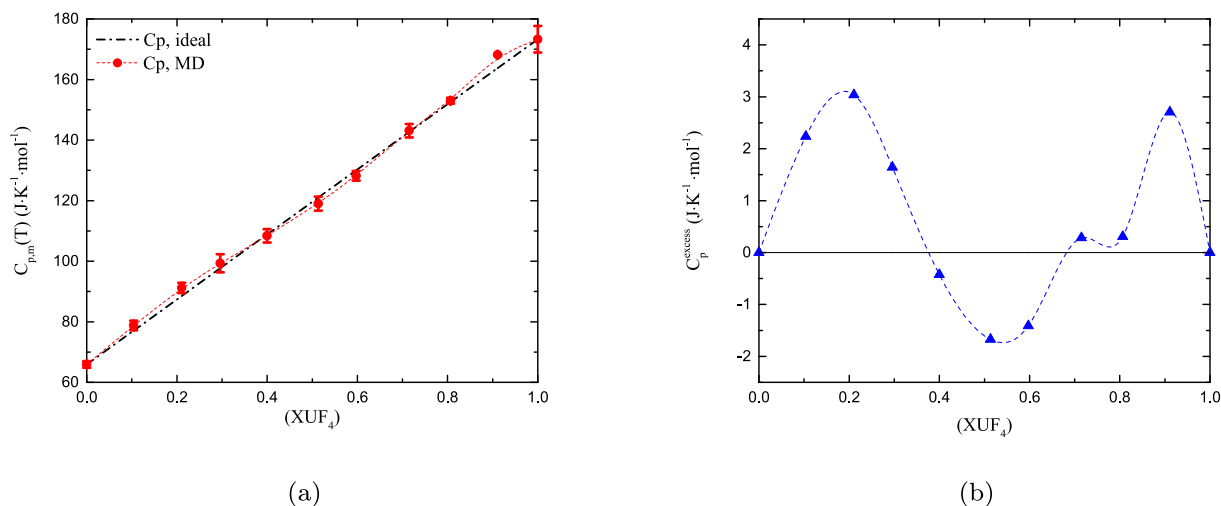


Fig. 12. (a) Heat capacity of the $(Li,U)F_x$ solution as calculated via MD (red) in the 900–1400 K temperature range, compared to the ideal heat capacity (black dashed line) obtained from the experimental heat capacities of the end-members (see Table 4 also). (b) Excess heat capacity of the $(Li,U)F_x$ solution derived from MD simulations.

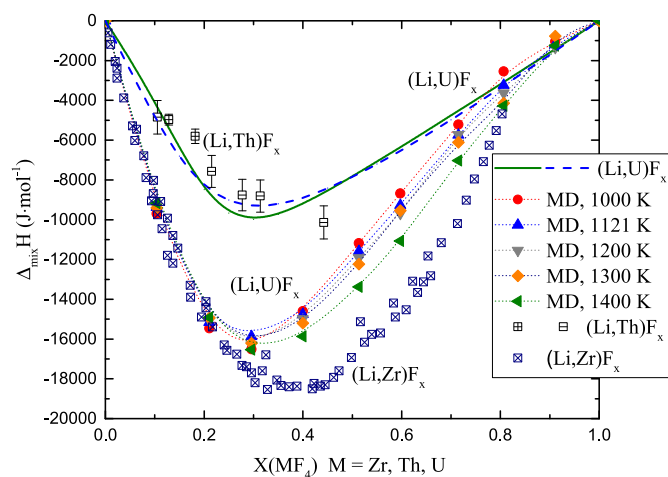


Fig. 13. Enthalpy of mixing of the $(Li,U)F_x$ solution as calculated at $T = 1400$ K with the present CALPHAD model (solid green line), and with the model by Beneš et al. [7], (blue dashed line). Mixing enthalpies for the same system at different temperatures (900–1400 K) were also calculated with MD, shown with symbols as indicated in the legend. Also shown are experimental measurements of the $(Li,Th)F_x$ solution at $T = 1121$ K, (□) and 1383 K (◻) [11], and the $(Li,Zr)F_x$ solution at 1150 K (◻) [70].

positive excess volume reveals. This is probably due to the solvation of Li^+ , which is nevertheless small enough to allow extended network formation. Indeed, in the 20 to 30 mol% region the degree of polymerization rapidly increases, reaching a fraction of about 0.9 by 30 mol% (see Fig. 10a, b).

The thermal expansion (shown in the Electronic Supporting Information, ESI), calculated from the density, showed a linear dependence in temperature, and the expansion decreases as a function of UF_4 content. Network formation is likely to account for this, since there is a greater bond strength between neighboring U^{4+} ions. The fits of the linear variations with temperature are listed in the ESI.

6.3.2. Heat capacity

Enthalpies were extracted directly from the ensemble averages of the potential energy of 0.5 ns NPT production runs at several temperatures: 900 K, 1000 K, 1121 K, 1200 K, 1300 K, and 1400 K. For every composition studied, a linear evolution of the molar enthalpy vs.

temperature was obtained (see ESI). Taking linear fits of the molar enthalpies, the heat capacity could then be calculated from:

$$C_{p,m} = \left(\frac{\partial H_m}{\partial T} \right)_p \quad (20)$$

The heat capacities of the end-members are very well reproduced: 65.9 vs. 64.183 [17] J·mol⁻¹·K⁻¹ (LiF) and 173.3 vs. 174.4 [34] J·mol⁻¹·K⁻¹ (UF_4). The heat capacity as a function of composition as calculated via MD is compared to the ideal heat capacity. Fig. 12a and b show that the heat capacity extracted from MD simulations has small deviations from additivity: much like the density, the heat capacity of the mixtures is close to ideal. For an industrial application setting this is convenient, since a reliable estimate can easily be made for both properties.

6.3.3. Mixing enthalpy, entropy and Gibbs energy

Plotted in Fig. 13 are the enthalpies of mixing at different temperatures (1000–1400 K) extracted from the MD simulations. Although the magnitude is likely overestimated, the negative excess at all compositions and position of the minima near $X(UF_4) = 0.3$ are reproduced at all temperatures. The Gibbs energies of mixing display similar trends to the mixing enthalpies, as the mixing entropies also contribute to favorable mixing (see ESI). The shape of the mixing entropy curve (ESI) in $(Li,U)F_x$ as calculated with the structural-thermodynamic model is somewhat closer to ideal mixing entropy than that of $(Li,Th)F_x$, yet with significant asymmetry and an inflection point near $X(UF_4) = 0.2$ which corresponds to the strong SRO evidenced by the rapidly rising ‘polymer’ fraction (see Fig. 10b).

Several calorimetric measurements reveal that the enthalpy of mixing in binary molten salt systems is usually negative (LiF- BeF_2 being a notable exception, with an S-shaped curve [71]) [11,70,72–74]. This is also the case for the LiF- UF_4 system according to our MD simulations, coupled structural-thermodynamic model, and the optimization previously reported by Beneš et al. [7] (Fig. 13). Daneš [75], suggested four main reasons to account for this behavior: i) change in the Coulombic repulsion energy of cations, ii) small structural changes during mixing, iii) no change in the number of first-nearest neighbors, iv) change in the state of ion polarization. In the LiF- UF_4 system, effect i) is probably the dominant one given that the uranium cation is tetravalent, and effect iii) is also likely to play a major role, as U^{4+} remains 7, 8, and 9-coordinated when dissolved in LiF (Section 6.2.2), with Li^+ only loosely associated in the second shell.

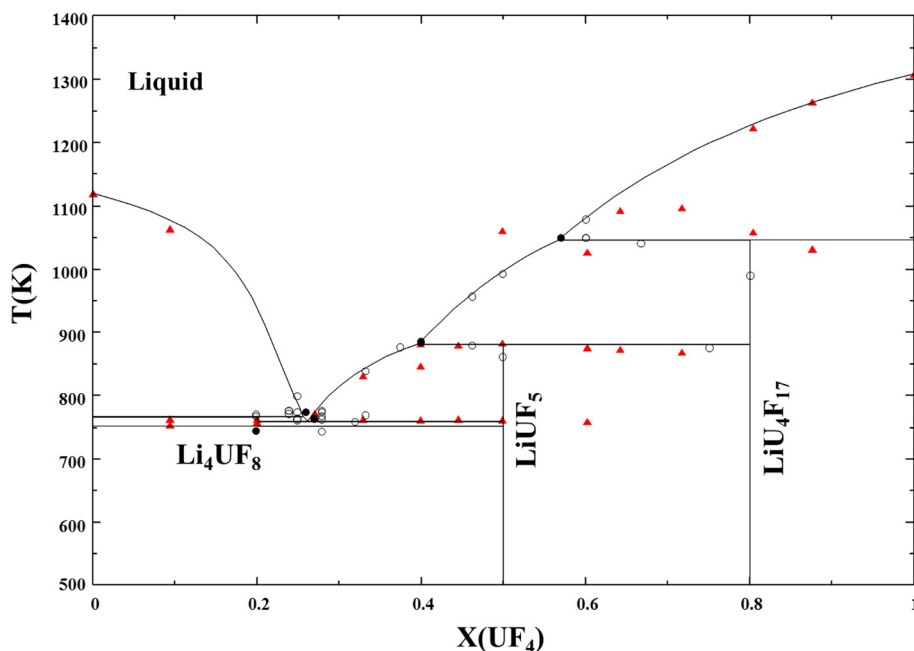


Fig. 14. LiF-UF₄ phase diagram as calculated in this work, superimposed against experimental points by Barton et al. (○,●) [5] and this study (▲, red, see also Table 7).

The speciation of the complexes, however, does vary (Table 11). In contrast, considering the loss of the network-like structure going from pure UF₄(l) to LiF(l), the overall structural changes are not so small and effect ii) probably contributes little to the negative enthalpy in this system. Effect iv) would become more evident by changing the alkali second-nearest neighbor, as the polarization ability of the alkali metals reduces down the alkali metal family. This will be studied in more detail in coming works.

Although there is no data on the mixing enthalpy of LiF-UF₄, its magnitude, calculated from the thermodynamic models (the present structural-thermodynamic and that of Beneš), is very similar to that of LiF-ThF₄, for which experimental measurements and thermodynamic calculations are available (Fig. 13). It is expected that the mixing enthalpy will be more negative across AF-UF₄ (A = alkali metal) with increasing radius of the alkali ion, as has been observed in many systems and in particular AF-ZrF₄ [70] and AF-ThF₄ [11,76] (although more measurements are needed, e.g. in the RbF and CsF-based systems). More

interesting is the influence of the tetravalent cation. Substituting Zr⁴⁺ (r_{ionic}~0.78 Å [57]) with Th⁴⁺ (r_{ionic}~1.05 Å [57]) results in a less negative excess mixing enthalpy as can be seen in Fig. 13. The more negative excess in the (Li,Zr)_x solution is related to the higher stability of [ZrF₂]^{4-z} anions with respect to [ThF₂]^{4-z} ones, and their reduced tendency to form Zr-F-Zr bridges [50]. The tendency towards a less negative deviation from ideal behavior with increasing size of the multivalent cation has been observed in other AX-MX_n systems [75]. Thus, the actinide contraction effect given by the substitution of Th⁴⁺ by U⁴⁺ likely results in a more negative deviation from ideality, which may be offset to some extent by the larger polarizability of Th⁴⁺.

6.4. CALPHAD assessment of the LiF-UF₄ system

The LiF-UF₄ binary system shown in Fig. 14 was optimized using both structural (Section 6.2) and calorimetric data from the literature and measured in this work by DSC (Table 7). Regarding the structural

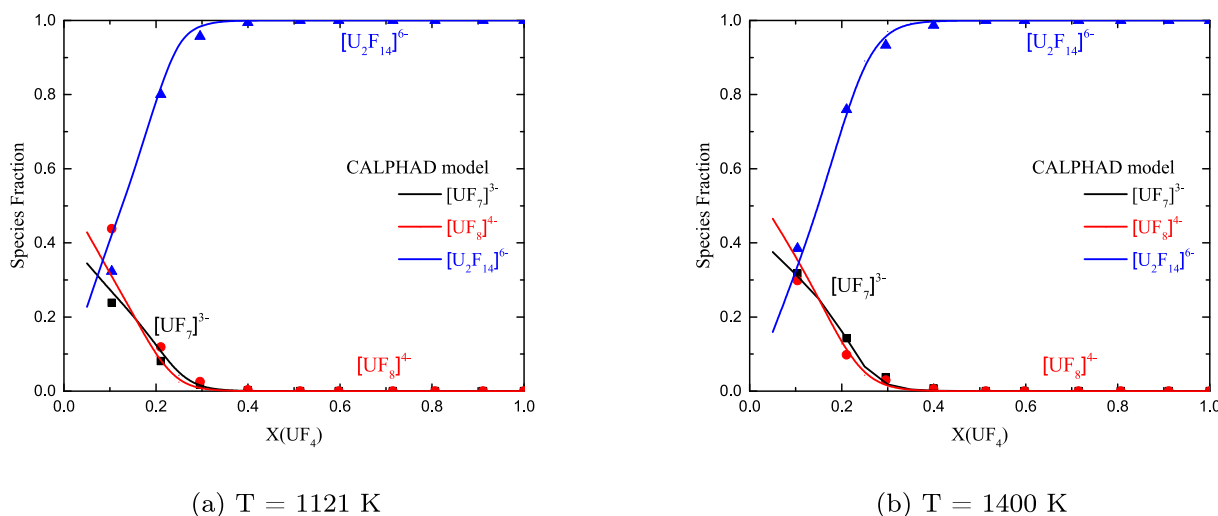


Fig. 15. Complex anion distribution obtained with the CALPHAD model (solid lines) and compared with the MD data shown in Table 10 (symbols): [UF₇]³⁻ (black), [UF₈]⁴⁻ (red), and [U₂F₁₄]⁶⁻ (blue). (a) T = 1121 K. (b) T = 1400 K.

data, the complex anion distribution of the main species $[\text{UF}_7]^{3-}$, $[\text{UF}_8]^{4-}$, and $[\text{U}_2\text{F}_{14}]^{6-}$ could be reproduced accurately, as shown in Fig. 15a, b. Recall that for modelling purposes, $[\text{U}_2\text{F}_{14}]^{6-}$ species encompass dimers, trimers, and polymers. The calculated phase diagram is also in agreement with the data gathered in the present work and with the data from Barton et al. [5]. The invariant equilibria are summarized in Table 6. The system is characterized by the formation of three ternary salts, all of which melt incongruently and at higher temperatures with increasing UF_4 content: Li_4UF_8 , LiUF_5 , and $\text{LiU}_4\text{F}_{17}$, and the existence of a fourth meta-stable phase with formula Li_3UF_7 (not visible on the calculated phase diagram). The melt is characterized by a predominance of hepta, octa, and nona-coordinated $[\text{UF}_x]^{4-x}$ complexes which remain isolated or form dimers, trimers, and chains of higher nuclearity through fluoride bridging, 'polymers'. Near $X(\text{UF}_4) = 0.4$, the solution is saturated with these polymeric chains, and remains so until the end-member UF_4 . This evolution is rather insensitive to temperature, at least until 1400 K, which was the maximum temperature studied here.

7. Conclusions

A structural and thermodynamic study of the $\text{LiF}-\text{UF}_4$ binary system is reported herein, in light of its relevance for MSR technology. The study set out two main objectives: i) confirm decades-old phase equilibria reported by Barton et al. [5] on which state-of-the-art MSR thermochemistry relies, ii) understand the structure of the molten salt as a function of composition, so as to link it with thermo-chemical properties and use it as input to develop a coupled structural-thermodynamic model. With regard to the first objective, it was found that the phase diagram proposed by Barton et al. is essentially correct, except for the phase with $\text{LiF}:\text{UF}_4 = 7:6$ stoichiometry which was found by other authors to be LiUF_5 . It was also confirmed that Li_3UF_7 is a meta-stable phase, and it is suggested to belong to the space group $P4/ncc$ like the isostructural Li_3ThF_7 compound. Following Cousson and Pages [44], who narrowed down the possible space groups of $\text{LiU}_4\text{F}_{17}$ to three ($I4/m$, $I4$, $I\bar{4}$), it was found from a LeBail refinement that the most probable one is $I4$. Further work could aim to obtain these intriguing phases with high purity and elucidate their crystal structures (the structure of $\text{LiTh}_4\text{F}_{17}$ also remains unknown).

The second objective relied on EXAFS spectroscopy as an experimental technique. Measurements were carried out at three compositions about 50 K above the liquidus temperature: $X(\text{UF}_4) = 0.25, 0.50$, and 0.67 . Fitting of the standard EXAFS equation as well as MD simulations were used to interpret the EXAS measurements, while it was possible to extend the composition and temperature space of analysis with the latter technique. The calculations, in agreement with other sources in the literature, showed that $(\text{Li,U})\text{F}_x(l)$ is a melt dominated by three coordination complexes throughout the entire composition range: $[\text{UF}_7]^{3-}$, $[\text{UF}_8]^{4-}$, and $[\text{UF}_5]^{9-}$, able to form a network of face, edge, or corner-sharing polyhedra. An advanced thermodynamic assessment was able to reproduce the distribution of $[\text{UF}_7]^{3-}$, $[\text{UF}_8]^{4-}$, and species of higher nuclearity accounted for by the $[\text{U}_2\text{F}_{14}]^{6-}$ dimer as calculated with MD simulations, while maintaining sound phase equilibria. Actinide contraction is apparent when the melt is compared to its $(\text{Li,Th})\text{F}_x$ analogue, although there do not seem to be significant changes between the excess properties of both systems. It remains to be seen if in other alkali fluoride-based systems the variability is more evident.

CRedit authorship contribution statement

J.A. Ocádiz-Flores: Conceptualization, Methodology, Investigation, Formal analysis, Visualization, Data curation, Writing - original draft. **A.E. Gheribi:** Investigation, Software, Formal analysis, Resources, Writing - review & editing. **J. Vlieland:** Investigation. **K. Dardenne:** Investigation. **J. Rothe:** Investigation. **R.J.M. Konings:** Conceptualization, Supervision, Writing - review & editing. **A.L. Smith:** Conceptualization,

Methodology, Investigation, Supervision, Funding acquisition, Resources, Project administration, Writing - review & editing.

Declaration of Competing Interest

The authors declare that they have no known competing financial interests or personal relationships that could have appeared to influence the work reported in this paper.

Acknowledgements

A.L. Smith acknowledges financial support from the Netherlands Organisation for Scientific Research (NWO) (project 722.016.005). J.A. Ocádiz-Flores acknowledges CONACYT-SENER for financial support. The authors would like to thank Mathieu Salanne for helpful discussions and for pointing out the PhD dissertation by Leslie Dewan on which they relied for the MD part of this work. The authors acknowledge the KIT light source for provision of instruments at the beamline INE of the Karlsruhe Institute of Technology (KIT) and would like to thank the Institute for Beam Physics and Technology (IBPT) for the operation of the storage ring, the Karlsruhe Research Accelerator.

Appendix A. Supplementary data

Supplementary data to this article can be found online at <https://doi.org/10.1016/j.molliq.2021.115820>.

References

- [1] E.S. Bettis, R.W. Schroeder, G.A. Cristy, H.W. Savage, R.G. Affel, L.F. Hemphill, Nucl. Sci. Eng. 2 (6) (1957) 804–825.
- [2] P.N. Haubenreich, J.R. Engel, Nucl. Technol. 8 (2) (1970) 118–136.
- [3] GIF, Annual report 2013, Generation IV International Forum, Tech. Rep. www.gen-4.org/gif/upload/docs/application/pdf/2014-06/gif_2013_annual_report-final.pdf 2013.
- [4] R.E. Thoma, Oak Ridge National Lab., Tenn., Technical report, 1971.
- [5] C.J. Barton, H.A. Friedman, W.R. Grimes, H. Inslay, R.E. Moore, R.E. Thoma, J. Am. Ceram. Soc. 41 (2) (1958) 63–69.
- [6] H.L. Lukas, S.G. Fries, B. Sundman, Computational Thermodynamics, The Calphad Method, Cambridge University Press, 2007.
- [7] O. Beneš, M. Beilmann, R.J.M. Konings, J. Nucl. Mater. 405 (2) (2010) 186–198.
- [8] S. Delpech, E. Merle-Lucotte, D. Heuer, M. Allibert, V. Ghetta, C. Le-Brun, X. Doligez, and G. Picard, J. Fluor. Chem. 130(1) (2009) 11–17. Fluorine Nuclear Energy.
- [9] Z. Dai, in: T.J. Dolan (Ed.), In Molten Salt Reactors and Thorium Energy, Woodhead Publishing 2017, pp. 531–540.
- [10] L. Jorgensen, In Molten Salt Reactors and Thorium Energy, Elsevier, 2017 557–564.
- [11] E. Capelli, O. Beneš, M. Beilmann, R.J.M. Konings, J. Chem. Thermodyn. 58 (2013) 110–116.
- [12] P.A. Madden, M. Wilson, Chem. Soc. Rev. 25 (5) (1996) 339–350.
- [13] P. Jemmer, M. Wilson, P.A. Madden, P.W. Fowler, J. Chem. Phys. 111 (5) (1999) 2038–2049.
- [14] L. Dewan, C. Simon, P.A. Madden, L.W. Hobbs, M. Salanne, J. Nucl. Mater. 434 (1) (2013) 322–327 Spec. Sect. Spent Nuclear Fuel.
- [15] R.J. Heaton, R. Brookes, P.A. Madden, M. Salanne, C. Simon, P. Turq, J. Phys. Chem. B 110 (23) (2006) 11454–11460.
- [16] A.L. Smith, E. Capelli, R.J.M. Konings, A.E. Gheribi, J. Mol. Liq. 299 (2020) 112165.
- [17] M.W. Chase, NIST-JANAF Thermochemical Tables (Journal of Physical and Chemical Reference Data Monograph No. 9), 1998.
- [18] P. Souček, O. Beneš, B. Claux, E. Capelli, M. Ougier, V. Tyrpekl, J.F. Vigier, R.J.M. Konings, J. Fluor. Chem. 200 (2017) 33–40.
- [19] J. Rodriguez-Carvajal, Physica B 192 (1993) 55–69.
- [20] O. Beneš, R.J.M. Konings, S. Wurzer, M. Sierig, A. Dockendorf, Thermochim. Acta 509 (1–2) (2010) 62–66.
- [21] G.W.H. Höhne, H.K. Cammenga, W. Eysel, E. Gmelin, W. Hemminger, Thermochim. Acta 160 (1) (1990) 1–12.
- [22] H.K. Cammenga, W. Eysel, E. Gmelin, W. Hemminger, G.W.H. Höhne, S.M. Sarge, Thermochim. Acta 219 (1993) 333–342.
- [23] W.J. Boettinger, U.R. Kattner, K.W. Moon, J.H. Perepezko, in: J.-C. Zhao (Ed.), In Methods for Phase Diagram Determination, Elsevier Science Ltd, Oxford 2007, pp. 151–221.
- [24] J. Rothe, S. Butorin, K. Dardenne, M.A. Denecke, B. Kienzler, M. Löble, V. Metz, A. Seibert, M. Steppert, T. Vitova, et al., Rev. Sci. Instrum. 83 (4) (2012) 043105.
- [25] A.L. Smith, M.N. Verleg, J. Vlieland, D. de Haas, J.A. Ocádiz-Flores, P. Martin, J. Rothe, K. Dardenne, M. Salanne, A.E. Gheribi, et al., J. Synchrotron Radiat. 26 (1) (2019).
- [26] B. Ravel, M. Newville, J. Synchrotron Radiat. 12 (4) (2005) 537–541.
- [27] M. Salanne, B. Rotenberg, S. Jahn, R. Vuilleumier, C. Simon, P.A. Madden, Theor. Chem. Accounts 131 (3) (2012) 1143.

- [28] M. Salanne, C. Simon, Pierre Turq, Robert J. Heaton, P.A. Madden, *J. Phys. Chem. B* 110 (23) (2006) 11461–11467.
- [29] O. Pauvert, M. Salanne, D. Zanghi, C. Simon, S. Reguer, D. Thiaudière, Y. Okamoto, H. Matsuura, C. Bessada, *J. Phys. Chem. B* 115 (29) (2011) 9160–9167.
- [30] L. Dewan, Molecular dynamics simulation and topological analysis of the network structure of actinide-bearing materials. PhD thesis, Massachusetts Institute of Technology, 2013.
- [31] K.T. Tang, J.P. Toennies, *J. Chem. Phys.* 80 (8) (1984) 3726–3741.
- [32] C.W. Bale, E. Bélsisle, P. Chartrand, S.A. Decterov, G. Eriksson, A.E. Gheribi, K. Hack, I.-H. Jung, Y.-B. Kang, J. Melançon, A.D. Pelton, S. Petersen, C. Robelin, J. Sangster, P. Spencer, M.-A. Van Ende, *Calphad* 54 (2016) 35–53.
- [33] J. Leitner, P. Voňka, D. Sedmidubský, P. Svoboda, *Thermochim. Acta* 497 (1–2) (2010) 7–13.
- [34] R.J.M. Konings, J.P.M. Van der Meer, E. Walle, European Commission Joint Research Centre, 2005.
- [35] A.D. Pelton, S.A. Decterov, G. Eriksson, C. Robelin, Y. Dessureault, *Metall. Mater. Trans. B* 31 (4) (2000) 651–659.
- [36] A.S. Dworkin, *J. Inorg. Nucl. Chem.* 34 (1) (1972) 135–138.
- [37] A.D. Pelton, P. Chartrand, *Metall. Mater. Trans. A* 32 (6) (2001) 1355–1360.
- [38] C.F. Weaver, R.E. Thoma, H. Insley, H.A. Friedman, Oak Ridge National Lab., Tenn., Technical report, 1959.
- [39] G. Brunton, *J. Inorg. Nucl. Chem.* 29 (7) (1967) 1631–1636.
- [40] A. Cousson, M. Pagès, R. Chevalier, *Acta Crystallogr. B* 34 (6) (1978) 1776–1778 Jun.
- [41] L.A. Harris, G.D. White, R.E. Thoma, *J. Phys. Chem.* 63 (11) (1959) 1974–1975.
- [42] G. Brunton, *Acta Crystallogr.* 21 (5) (1966) 814–817.
- [43] Y. Jeongho, M.D. Smith, J. Tapp, A. Möller, H.C. Zur Loye, *Inorg. Chem.* 53 (12) (2014) 6289–6298.
- [44] A. Cousson, M. Pages, J.C. Cousseins, A. Vedrine, *J. Cryst. Growth* 40 (1) (1977) 157–160.
- [45] A.L. Ankudinov, B. Ravel, J.J. Rehr, S.D. Conradson, *Phys. Rev. B* 58 (12) (1998) 7565.
- [46] P.A. Lee, J.B. Pendry, *Phys. Rev. B* 11 (8) (1975) 2795.
- [47] A. Filipponi, *J. Phys. Condens. Matter* 13 (7) (2001) R23.
- [48] R.A. Penneman, R.R. Ryan, A. Rosenzweig, *In Rare Earths*, Springer, 1973 1–52.
- [49] L.M. Toth, *J. Phys. Chem.* 75 (5) (1971) 631–636.
- [50] C. Bessada, D. Zanghi, M. Salanne, A. Gil-Martin, M. Gibilaro, P. Chamelot, L. Massot, A. Nezu, H. Matsuura, *J. Mol. Liq.* 307 (2020) 112927.
- [51] J.A. Ocadiz-Flores, A.E. Gheribi, J. Vlieland, D. de Haas, K. Dardenne, J. Rothe, R.J.M. Konings, A.L. Smith, Unpublished Manuscript, 2020.
- [52] R.J. Heaton, P.A. Madden, *Mol. Phys.* 106 (12–13) (2008) 1703–1719.
- [53] J.B. Liu, X. Chen, Y.H. Qiu, C.F. Xu, W.H. Eugen Schwarz, J. Li, *J. Phys. Chem. B* 118 (48) (2014) 13954–13962.
- [54] J. Dai, D. Long, P. Huai, Q. Li, *J. Mol. Liq.* 211 (2015) 747–753.
- [55] S. Kern, J. Hayward, S. Roberts, J.W. Richardson Jr., F.J. Rotella, L. Soderholm, B. Cort, M. Tinkle, M. West, D. Hoisington, et al., *J. Chem. Phys.* 101 (11) (1994) 9333–9337.
- [56] G.V. Girichev, A.V. Krasnov, N.I. Giricheva, O.G. Krasnova, *J. Struct. Chem.* 40 (2) (1999) 207.
- [57] R.D. Shannon, *Acta Crystallographica A* 32 (5) (1976) 751–767.
- [58] M.A. Howe, R.L. McGreevy, W.S. Howells, *J. Phys. Condens. Matter* 1 (22) (1989) 3433.
- [59] I. Okada, H. Okano, H. Ohtaki, R. Takagi, *Chemical, Phys. Lett.* 100 (5) (1983) 436–441.
- [60] F. Lantelme, P. Turq, The, *J. Chem. Phys.* 77 (6) (1982) 3177–3187.
- [61] C. Caccamo, M. Dixon, *J. Phys. C Solid State Phys.* 13 (10) (1980) 1887.
- [62] I. Okada, R. Takagi, K. Kawamura, *Zeitschrift für Naturforschung A* 35 (5) (1980) 493–499.
- [63] M.M. Walz, D. Van der Spoel, *Phys. Chem. Chem. Phys.* 21 (34) (2019) 18516–18524.
- [64] Y. Abe, O. Kosugiyama, A. Nagashima, *J. Nucl. Mater.* 99 (2–3) (1981) 173–183.
- [65] Y.F. Chervinskij, V.N. Desyatnik, A.I. Nechaev, *Zhurnal Fizicheskoy Khimii* 56 (8) (1982) 1946–1949.
- [66] V.N. Desyatnik, A.I. Nechaev, Y.F. Chervinskii, *Zh. Fiz. Khim., USSR*, 53, 1979 4.
- [67] A.A. Klimenkov, N.N. Kurbatov, S.P. Raspopin, Y.F. Chervinskii, *Atomic Energy* 56 (5) (1984) 339–341.
- [68] L.V. Jones, K.C. Jordan, R.W. Joyner, E.L. Murphy, B.C. Blanke, E.N. Bousquet, Technical Report USAEC MLM-1086, 1956.
- [69] B. Porter, R.E. Meaker, Technical Report BMI RI-6836, 1966.
- [70] G. Hatem, F. Tabaries, M. Gaune-Escard, *Thermochim. Acta* 149 (1989) 15–26.
- [71] J.L. Holm, O.J. Kleppa, *Inorg. Chem.* 8 (2) (1969) 207–212.
- [72] G.N. Papatheodorou, O.J. Kleppa, *J. Inorg. Nucl. Chem.* 32 (3) (1970) 889–900.
- [73] G.N. Papatheodorou, O.J. Kleppa, *J. Inorg. Nucl. Chem.* 33 (5) (1971) 1249–1278.
- [74] J.L. Holm, O.J. Kleppa, *J. Chem. Phys.* 49 (5) (1968) 2425–2430.
- [75] V. Danek, *Physico-Chemical Analysis of Molten Electrolytes*, Elsevier, 2006.
- [76] J.A. Ocadiz-Flores, E. Carré, J.-C. Griveau, E. Colineau, E. Capelli, P. Souček, O. Beneš, R.J.M. Konings, A.L. Smith, *J. Chem. Thermodyn.* 145 (2020) 106069.